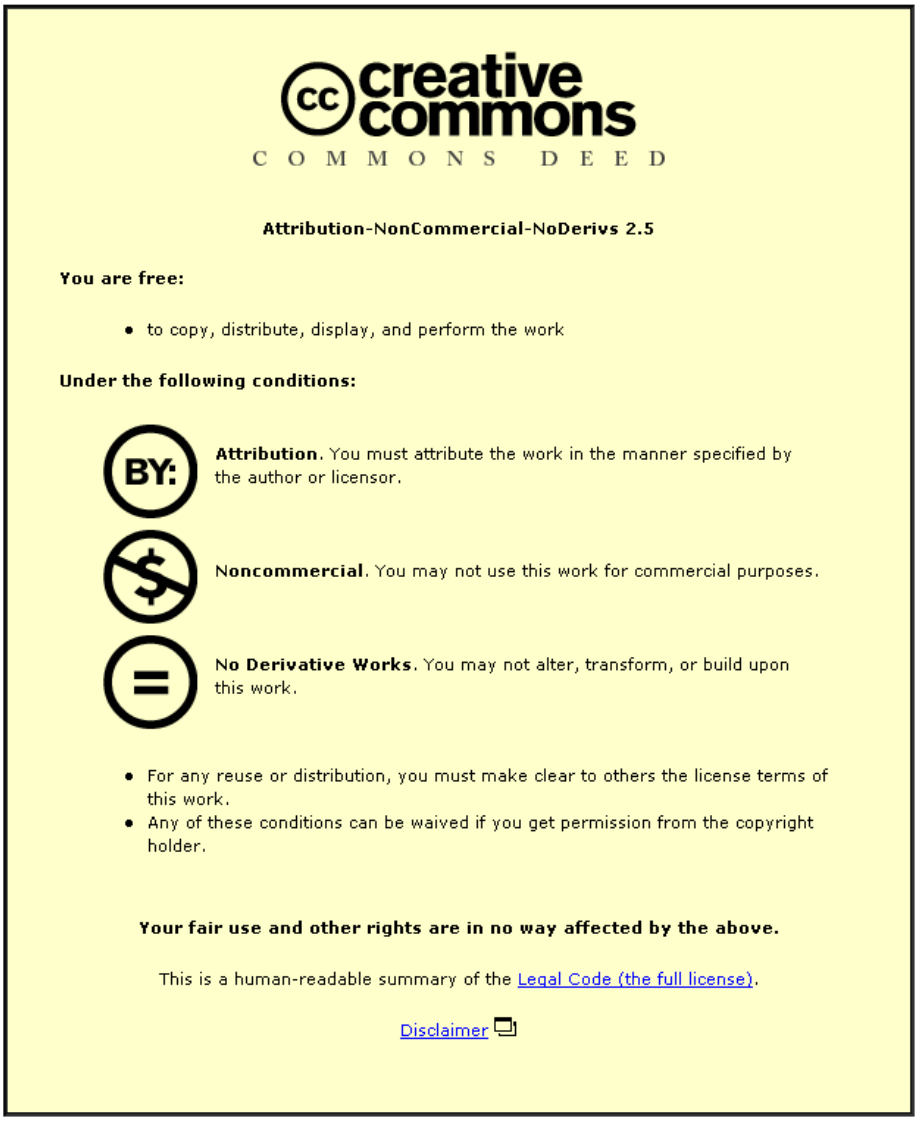

creative commons

COMMONS DEED

Attribution-NonCommercial-NoDerivs 2.5

You are free:

- to copy, distribute, display, and perform the work

Under the following conditions:

Attribution. You must attribute the work in the manner specified by the author or licensor.

Noncommercial. You may not use this work for commercial purposes.

No Derivative Works. You may not alter, transform, or build upon this work.

- For any reuse or distribution, you must make clear to others the license terms of this work.
- Any of these conditions can be waived if you get permission from the copyright holder.

Your fair use and other rights are in no way affected by the above.

This is a human-readable summary of the Legal Code (the full license).

Disclaimer

Citation:
Odedra, A and W. Malalasekera, Eulerian Particle Flamelet Modelling of a Bluff-body CH4/H2 Combustion and Flame, Volume 151, Issue 3, November 2007, Pages 512-531, DOI:10.1016/j.combustflame.2007.06.018.

Title: **Eulerian Particle Flamelet Modelling of a Bluff-body CH_4/H_2 Flame**

Article: Full-length

1st Author: Anand Odedra

Affiliation: Loughborough University

Address: Wolfson School of Mechanical and Manufacturing Engineering, Loughborough University, Loughborough, UK, LE11 3TU.
Phone: +44 (0) 1509 227520
Fax : +44 (0) 1509 227648
E-mail: A.Odedra@lboro.ac.uk

2nd Author: W. Malalasekera (Corresponding author)

Affiliation: Loughborough University

Address: Wolfson School of Mechanical and Manufacturing Engineering, Loughborough University, Loughborough, UK, LE11 3TU.
Phone: +44 (0) 1509 227556
Fax : +44 (0) 1509 227648
E-mail: W.Malalasekera@lboro.ac.uk

MODIFIED – 02.07.2007

Submitted to Combustion and Flame – November 2005, Revised - December 2006, February 2007 and July 2007.

Abstract

In this paper an axisymmetric RANS simulation of a bluff-body stabilised flame has been attempted using steady and unsteady flamelet models. The unsteady effects are considered in a post-processing manner through the Eulerian Particle Flamelet Model (EPFM). In this model the transient history of scalar dissipation rate, conditioned at stoichiometric mixture fraction is required to generate unsteady flamelets and obtained by tracing Eulerian particles. In this approach unsteady convective-diffusive transport equations are solved to consider the transport of Eulerian particles in the domain. Comparisons of the results of steady and unsteady calculations show that transient effects do not have much influence on major species, including OH and the structure of the flame therefore can be successfully predicted by steady or unsteady approaches. However, it appears that slow processes like NO formation can only be captured accurately if unsteady effects are taken into account while steady simulations tend to overpredict NO. In this work turbulence has been modelled using the Reynolds Stress Model (RSM). Predictions of velocity, velocity rms, mean mixture fraction and its rms show very good agreement with experiments. Performance of three detailed chemical mechanisms, the GRI Mech 2.11, the San Diego mechanism and the GRI Mech 3.0 has also been evaluated in this study. All three mechanisms performed well with both steady and unsteady approaches and produced almost identical results for major species and OH. However, the difference between mechanisms and flamelet models becomes clearly apparent in the NO predictions. The unsteady model incorporating the GRI Mech 2.11 provided better predictions of NO compared to steady calculations and showed close agreement with experiments. The other two mechanisms showed overpredictions of NO with both unsteady and steady models. The level of overprediction is severe with the steady approach. The GRI Mech 3.0 appears to overpredict NO by a factor of two compared to GRI Mech 2.11. The NO predictions by the San Diego mechanism fall between the two GRI mechanisms. The present study demonstrates the success of the EPFM model and when used with the GRI 2.11 mechanism predicts all flame properties, major and minor species very well and most importantly the correct NO levels.

1. Introduction

There are several well-established and validated mathematical models available to model turbulent nonpremixed combustion. These include steady laminar flamelet model (SLFM) [1, 2, 3], PDF transport model [4] and the conditional moment closure model (CMC) [5, 6]. The steady laminar flamelet model has become more popular than other methods because it offers a convenient mechanism for incorporating realistic chemical kinetics into the calculation of nonpremixed flames. In the standard flamelet model three parameters, mean mixture fraction $\tilde{\xi}$, its variance $\tilde{\xi}''^2$ and mean scalar dissipation rate $\tilde{\chi}$ (a measure of flame stretch) are used to specify the local instantaneous thermo-chemical state in the turbulent flow. In the steady flamelet model the time-dependent term is neglected assuming slow variation of imposed scalar dissipation rate to generate a parameterized library of flamelet profiles. However, if the scalar dissipation rate changes rapidly then the unsteady term in the flamelet equations becomes important leading to slow relaxation of the flamelet profiles [3] which is the basis of the unsteady flamelet formulation. The steady flamelet model successfully predicts major species and certain minor species in some cases but clearly fails to capture slow processes like NO_x formation.

The importance of unsteady effects in stretched laminar flamelet models for turbulent nonpremixed flames was first identified by Haworth *et al*. [7]. The study showed that the look-up table solution of steady flamelet equations is not always justified as flamelet structure cannot respond instantaneously to the scalar dissipation changes. Mauss *et al.* [8] have used transient flamelets to simulate extinction and re-ignition in turbulent diffusion jet flames and showed that flamelets respond much more slowly to changes in scalar dissipation rate than previously assumed. The Representative Interactive Flamelet (RIF) concept developed by Peters and co-workers [3, 9, 10] is an interactive extension of the laminar flamelet model and accounts for the transient history of the scalar dissipation rate. It computes the unsteady flamelet equations interactively within the main CFD code. The transient evolution of a single or several 'representative' flamelets is considered in this model. Pitsch *et al*. [10] have employed the RIF model using a single representative flamelet in a three-dimensional diesel engine simulation and found reasonable agreement with experimental data for pressure, ignition delay, cylinder-averaged major species and exhaust gas emissions including NO and soot. In a further application of this model in

a diesel engine simulation, results have been shown to be improved by using multiple interactive flamelets [11].

Mainly there are two types of unsteady flamelet models that could be successfully implemented either interactively or applied in a post-processing manner, the Lagrangian Flamelet Model (LFM) [12] and the Eulerian Particle Flamelet Model (EPFM) [13]. In LFM, flamelets are assumed to be introduced at the nozzle inlet and allowed to convect downstream. An expression which relates the axial position of the flamelet to a Lagrangian flamelet lifetime is used to integrate flamelet equations thereby accounting for history effects in the flamelet structure. The EPFM traces mass weighted fractions of particles corresponding to flamelets, initialised at particular locations according to the stoichiometric mixture fraction value and the scalar dissipation field. The EPFM has the advantage that it accounts for spatial variation of the scalar dissipation rate in the evolution of multiple unsteady flamelets [11, 13]. Application of the LFM is limited to parabolic flows while the EPFM can be used for both parabolic and elliptical flows. The post-processing analysis is, however, valid only for steady combustion problems.

Barths *et al*. [14] have used the EPFM approach to simulate a gas turbine combustor operating in steady state. In their study good agreement for the NO_x index was obtained using the EPFM model but no detailed comparisons were available to asses the accuracy of local predictions. Later Coelho *et al*. [15] have applied EPFM to a piloted methane-air jet flame and found good agreement with experiments. They also studied the influence of the number of particles, initialisation regions and initial conditions on scalar predictions. In a further application Coelho *et al*. [16] have used the EPFM to model in a recirculating mild combustion burner but detailed comparisons of temperature and species were not available due to lack of experimental data. The present study uses the EPFM approach in a well documented experimental configuration where detailed experimental data is available to study the accuracy and capabilities of the EPFM strategy. The experimental configuration used here is the bluff-body stabilised CH_4/H_2 (HM1) flame investigated experimentally at Sandia National Laboratories and at the University of Sydney [17].

The HM1 flame has been the subject of a number of previous numerical studies. Among others, these include early studies of Dally *et al.* [18], Li *et al*. [19], Yan *et al*. [20], Hossain and Malalasekera [21] and Hossain *et al.* [22]. The flow field calculations using the $k-\varepsilon$ model for turbulence closure with a modified constant

$C_{\varepsilon 1}$ (from 1.44 to 1.6) in the dissipation equation has shown to achieve reasonably good agreement for the flow and scalar field. Improved flow field predictions have been reported with the use of Explicit Algebraic Stress Models (EASM), modified $k-\varepsilon$ [20] and Reynolds Stress Models (RSM) [19]. Studies which have used simple chemistry [18] and equilibrium chemistry [19] have shown limited success in predicting overall flame properties. The use of the laminar flamelet model [20, 21, 22] has been shown to give good predictions for major and minor species. In addition to major species predictions, Hossain and Malalasekera [21] have used the laminar flamelet model with a special procedure for NO and attempted to predict NO in this bluff-body flame. Only thermal NO was included in the chemical mechanism and the predicted results showed an under-prediction (with unity Lewis number assumption) compared to the experimental measurements.

Kim *et al*. [23] have applied a first-order CMC model to the HM1 flame and obtained good agreement for major species but minor species OH and NO were overpredicted. They have attributed discrepancies to the first-order accuracy of the CMC model and uncertainties involved in the chemical mechanisms. Later Sreedhara *et al*. [24] have modelled the same flame using a second-order elliptic CMC model and showed slight improvement in the predictions of OH and NO. Both studies [23, 24] have reported that the GRI Mech 3.0 overpredicts NO by a factor of two and noted that GRI Mech 2.11 provides better agreement.

Muradoglu *et al*. [25] have used the transported PDF model with a simple flamelet model to study the sensitivity of the calculations to boundary conditions and model constants. Their study was limited to the prediction of flow characteristics and the mixing field. More comprehensive PDF simulation for this bluff-body flame has been reported by Liu *et al* [26] who used a reduced mechanism for chemistry derived from GRI Mech 2.11. Their results show good agreement near the burner but agreement further downstream was not very good for mixture fraction fluctuations, temperature and species. More recently Kuan and Lindstedt [27] have used the transported PDF approach with a detailed chemistry mechanism, and the Reynolds stress model to model HM1 and HM1e flames. Their results show good agreement for major species and minor species CO, OH and NO. Slight over-predictions of NO were attributed to the adiabatic assumption which as made in this computation. The results

presented also include species fluctuation predictions (rms) and conditional PDFs of temperature and species including NO.

Recently Kempf *et al.* [28] and Raman and Pitsch [29] have reported Large Eddy Simulations (LES) for this burner configuration. Kempf *et al.* [28] have reported LES results using a grid which was sufficient to resolve more than 75% of total turbulent kinetic energy of the critical part of the flow field. The laminar flamelet model was used to obtain thermochemistry. The results showed reasonably good agreement for flow field data and subsequent temperature and major species predictions were also good. Raman and Pitsch [29] also used LES and the laminar flamelet model for thermochemistry and reported very good agreement with data. However the study reports that good mixture fraction could be only is achieved by tuning inlet boundary conditions. No prediction for NO_x was attempted in either of the studies. It is worth noting that LES is a very expensive and time consuming technique and in terms of application still is not an engineering tool.

Most CFD based combustion calculations used in the industry still use RANS based methodology and post-processing techniques for NO. In this work we use the EPFM formulation in the RANS framework to simulate a bluff-body CH_4/H_2 flame. In this work we compare our predictions for all major and minor species with experiments including NO_x and demonstrate that the current strategy is a cost effective way of accurately predicting the flame properties including NO_x.

The basics of laminar flamelet model and its extension to EPFM formulation are discussed in the next section. Then a brief overview of the experimental set-up used in the experiments considered for validation is given. Then the numerical implementation of post-processing type EPFM is described. It is followed by the model validation results using different chemical mechanisms and finally conclusions are summarised.

2. Mathematical Model

The modelling approach used in the present study follows the procedures outlined in Barths *et al* [11], Coelho and Peters [15, 16]. The study is divided into two stages. The first stage involves the solution of fluid flow and scalar transport equations (mean mixture fraction and its variance) and prediction of dependent scalar fields. Next the second stage of the calculations is performed in a post-processing

manner using the EPFM approach. In this work the governing equations of fluid flow are solved using the commercial CFD code FLUENT 6.1 [41]. Turbulence is modelled using the Reynolds Stress Model (RSM) in which the pressure strain term is approximated according to the linear model proposed by Launder [30, 31]. In this study we present results for both the steady laminar flamelet model and the EPFM approach and compare the results. The steady/unsteady laminar flamelets used in our calculations are obtained externally using the FlameMaster code [32]. In the first stage of the calculation procedure a converged SLFM solution is obtained using FLUENT. Then the density, mean mixture fraction and its variance predictions from the first stage are used to perform the second stage EPFM calculations. Further details are outlined below.

2.1 Steady Calculations

The steady laminar flamelet model used in this study is described in Pitsch and Pertes [33] The FlameMaster code [32] is used to generate the flamelet library for varying scalar dissipation rates ranging from a low value close to equilibrium up to a large value close to extinction ($0.0001s^{-1}$ to $55.47s^{-1}$ for the present case). The chemical mechanism used is GRI Mech 2.11. Pitsch *et al*. [12] have shown that steady flamelet calculations overpredict the radiation heat loss and give unrealistic temperature predictions therefore radiation is neglected in the steady laminar flamelet calculation. In the calculation process a three-dimensional look-up table containing $\tilde{\xi}$, $\tilde{\xi}''^2$ and $\tilde{\chi}$ is used to update density, temperature and other scalar properties. The Favre averaged mean values of the scalars are obtained by integrating over the flamelet profiles using the presumed probability density function approach [15]. In the calculation the probability density function, $\tilde{P}(\xi)$ is assumed to be a β-PDF.

2.2 Unsteady Calculations using EPFM

Unsteady calculations are performed as a post-processing stage after the steady calculations. As this is an uncoupled approach the mixing field (predicted mean and variance of the mixture fraction) and the scalar dissipation field are fixed at this stage. The turbulent mean values of scalars (temperature and chemical species) are computed in the post-processing stage employing the Eulerian Particle Flamelet Model (EPFM). In this model different marker particles representing flamelets are

introduced into the turbulent flow and transported throughout the flow domain. The probability of finding a fluid particle at a given location is calculated by solving an unsteady transport equation. Depending on the path of a particle takes through the turbulent flow field each particle represent a different flamelet history. Eulerian transport equation for the probability of finding a fluid particle representing a flamelet can be written as [35]

$$\bar{\rho}\frac{\partial \tilde{I}_n}{\partial t}+\bar{\rho}\frac{\partial\left(\tilde{u}_i\tilde{I}_n\right)}{\partial x_j}=\bar{\rho}\frac{\partial}{\partial x_j}\left(\frac{\mu_t}{\sigma_t}\frac{\partial \tilde{I}_n}{\partial x_j}\right) \tag{1}$$

In Eq. 1 $\widetilde{I}_n$ is the probability of finding a particle *n* and σ_t is the turbulent Prandtl number. As particles are transported through the domain they experience different values of the scalar dissipation rate, depending on their position within the flow field. A surface averaged value for the scalar dissipation rate conditioned at stoichiometric mixture for each particle is calculated following [12] by converting the surface integrals into volume integrals. Here it is weighted additionally with $\tilde{I}_n$ the probability of finding a particle *n* the resulting surface averaged scalar dissipation rate is given by [35]

$$\hat{\chi}_{st,n}=\frac{\int_V \tilde{I}_n\bar{\rho}\tilde{\chi}_{st}^{\,3/2}\tilde{P}\left(\xi_{st}\right)dV}{\int_V \tilde{I}_n\bar{\rho}\tilde{\chi}_{st}^{\,1/2}\tilde{P}\left(\xi_{st}\right)dV} \tag{2}$$

where $\tilde{\chi}_{st}$ is the scalar dissipation rate conditioned at stoichiometry [12]

$$\tilde{\chi}_{st}=\frac{\tilde{\chi}}{\int_0^1 \frac{f\left(\xi\right)}{f\left(\xi_{st}\right)}\tilde{P}\left(\xi\right)d\xi} \tag{3}$$

where mean scalar dissipation $\tilde{\chi}$ is modelled according to [34]

$$\tilde{\chi}=c_\chi\frac{\tilde{\varepsilon}}{\tilde{k}}\tilde{\xi}''^2 \tag{4}$$

where $\widetilde{k}$ is the turbulent kinetic energy, $\widetilde{\varepsilon}$ the dissipation rate of turbulent kinetic energy, $\tilde{\xi}''^2$ the mixture fraction variance and a constant $c_\chi = 2.0$ [3].

In Eq. 2 numerator and denominator are integrated over the whole computational domain. The surface averaged conditional scalar dissipation rate $\hat{\chi}_{st,n}$

is a function of time as the probability of finding a particle $\widetilde{I}_n$ changes with time. Equation 2 gives the transient history of the surface averaged scalar dissipation rate.

In the unsteady flamelet calculations radiation is accounted for by using the optically thin approximation with absorption coefficients calculated using RADCAL [40]. The rate of radiative heat loss per unit volume $\dot{q}_R''$ is computed as

$$\dot{q}_R'' = 2\sigma\left(T^4 - T_a^4\right)\sum_i p_i \alpha_{p,i} \tag{5}$$

where σ is the Stefan-Boltzmann constant, T_a the ambient temperature, p_i and $\alpha_{p,i}$ are the partial pressure and the absorption coefficient for species *i*, respectively. The species CO, CO_2, H_2O and CH_4 take part in radiation calculations.

The local steady-state Favre averaged mass fractions can be computed by integration over time and summation over the number of particles, weighted by the temporal integration of the summation over all marker particles [14]

$$\tilde{\phi}_i\left(\vec{x},t\right) = \frac{\sum_n \int_0^{t_{final}} \tilde{I}_n(t)\left(\int_0^1 \phi_i\left(\xi,\hat{\chi}_{st,n}\right)\tilde{P}(\xi)\,d\xi\right)dt}{\sum_n \int_0^{t_{final}} \tilde{I}_n(t)\,dt} \tag{6}$$

In Eq. 6 t_{final} is chosen long enough so that all the particles leave the reaction zone and their contribution to integral in Eq. 6 becomes negligible.

Temperature rms $\widetilde{T}'^2$ for the steady case is calculated via a simple integration of $\left(\widetilde{T} - T(\xi)\right)^2$ weighted by the PDF and for the unsteady case

$$\left(\tilde{T}'\right)^2 = \frac{\sum_n \int_0^{t_{final}} \tilde{I}_n(t)\left[\int_0^1 \left(\tilde{T}_n\left(\vec{x},t\right) - T_n\left(\xi\right)\right)^2 \tilde{P}(\xi)\,d\xi\right]dt}{\sum_n \int_0^{t_{final}} \tilde{I}_n(t)\,dt} \tag{7}$$

$$\tilde{T}_n\left(\vec{x},t\right) = \int_0^1 T_n\left(\xi\right)\tilde{P}(\xi)d\xi \tag{8}$$

where $T_n(\xi)$ is the temperature profile of unsteady laminar flamelet corresponding to $\hat{\chi}_{st,n}$.

3. Experimental Set-up

The experimental data used in the present study are from the Sydney bluff-body burner documented in [17, 18]. It has an outer diameter $D = 50$ mm with a concentric fuel jet diameter $d = 3.6$ mm. The complete burner assembly was housed in a square co-flow wind tunnel of cross-section 254×254 mm. The fuel used was 1:1 methane/hydrogen by volume with stoichiometric mixture fraction $\xi_{st} = 0.05$. The scalar fields were measured by single-point Raman-Rayleigh LIF (Laser Induced Fluorescence) at Sandia National Laboratories. For the HM1 flame the fuel jet velocity was 118m/s with a co-flow velocity of 40m/s. The velocity data were collected by LDV (Laser Doppler Velocimetry) at the University of Sydney for the HM1e case where fuel jet velocity was 108m/s and co-flow velocity was 35m/s. Flame HM1e is the equivalent flame to HM1. Wind tunnel at the Sydney University was unable to generate a uniform 40m/s co-flow (maximum 35m/s). Therefore the jet velocity was accordingly reduced from 118m/s to 108m/s so that both HM1 and HM1e are at the same proportion from blow-off.

4. Computational Details

Computational Grid and Boundary Conditions

Fig. 1 shows the axisymmetric computational grid used in the present study. The main domain (excluding upstream extension) is discretised using 170×260 quadrilateral cells. Close to the bluff-body the grid has been adequately refined to resolve the recirculation zone. Through grid refinement studies it was established that this grid is fine enough to provide grid independent flow predictions (see sample results later). The domain is extended upstream to calculate the correct velocity profile at the burner exit. The bulk velocities and 10 % turbulence intensity are specified as inlet boundary conditions of the extended domain. This approach eliminated the uncertainties involved in specifying velocity profiles and length scale at the burner exit and proved very successful as shown in the flow field comparisons later. Transport equations for velocities, combustion and turbulent quantities were discretised using the second-order upwind scheme and the SIMPLE algorithm was used for pressure-velocity coupling. Two different simulations were performed corresponding to the flow field and scalar measurements [36]. In the first simulation fuel jet velocity and co-flow velocity were set to 108 m/s and 35 m/s respectively.

Flow field results of this flame are compared with HM1e flame data. The second simulation used slightly higher jet velocity of 118 m/s and co-flow velocity of 40 m/s. The scalar predictions of this simulation are compared with HM1 measurements.

The EPFM Solution Algorithm

Schematic of the EPFM solution procedure which involves two stages is shown in Fig. 2. First stage CFD calculations are performed using FLUENT while second stage calculations are done separately in MATLAB. The first stage simulation took around 6 hrs of clock time and second stage EPFM calculations using one particle took roughly 3-4 hrs of actual time on a single processor, Pentium 4, 1 GB RAM machine. Post-processing calculations begin with a converged SLFM solution. The density, mean mixture fraction $\widetilde{\xi}$, its variance $\widetilde{\xi}''^2$ and mean scalar dissipation rate $\widetilde{\chi}$ values are used in the second stage to calculate conditional scalar dissipation rate $\widetilde{\chi}_{st}$ (Eq. 3) for each cell. An initialization region (computational cells) near to the fuel inlet where $\widetilde{\xi} > \widetilde{\xi}_{st}$ is selected [15]. If only one marker particle is considered, the initial probability $\tilde{I}_{n=1}$ is set equal to unity in the considered region and zero everywhere else. If multiple particles are considered, the initialization region remains the same, but it is divided into a number of sub-regions equal to the number of marker particles, and each sub-region is assigned to one particle [15]. The initial probability of finding a marker particle is then equal to 1 in its own sub-region and equal to 0 everywhere else. Different types of particles are separated by different initial conditions. At this stage only unsteady transport equations (Eq. 1) are solved using the flow field data. At each time iteration step probability of finding a particle n, $\widetilde{I}_n$ within the entire domain for each particle is obtained. Using $\widetilde{I}_n$ values at each cell and the conditional scalar dissipation value, a surface averaged conditional scalar dissipation rate, $\hat{\chi}_{st,n}$ can be calculated at each time step. This transient history of $\hat{\chi}_{st,n}$ is then used to compute unsteady flamelets in FlameMaster. The calculations of unsteady flamelet equations also require initial conditions, which are taken from the steady solution. For NO calculations, all the species involved with nitrogen chemistry except N_2 are initially set to zero. Finally the turbulent mean values of scalars are calculated employing Eq. 6. The steady flamelet results shown here for comparison

purposes were calculated in the post-processing stage using only one flamelet, corresponding to the steady state value of $\hat{\chi}_{st,n}$. Three different reaction mechanisms were used to generate steady and unsteady flamelets, GRI Mech 2.11 (49 species and 277 reactions [37]), GRI Mech 3.0 (53 species and 325 reactions [38]) and San Diego mechanism (53 species and 228 reactions [39]).

5. Results and Discussion

Figures 3a and 3b show calculated streamline contours for HM1e and HM1 cases respectively. The axial positions where experimental data were measured are also shown. Both flames exhibit similar flow characteristics. In both cases the recirculation zone is extended up to x/D = 1.8. Two vortices can be seen inside the recirculation zone. Eight measurement locations in the case of HM1e and four in the case of HM1 fall inside the recirculation zone. First we present flow field results for HM1e case. Fig. 4 shows comparison of axial velocity predictions with measurements. It can be seen that numerical results show excellent agreement at all the axial positions. The numerical results correctly predict the change of axial velocity direction indicating that the length and shape of the recirculation zone is predicted very well. Radial velocity comparisons in Fig. 5 show good agreement close to the burner except for slight under-predictions at downstream positions. Magnitude of the radial component is small and the discrepancies are not of similar size as the errors in the axial velocity profiles. The rms fluctuations of axial and radial velocity are presented in Fig. 6 and 7 respectively. Experimental data of axial velocity fluctuations show two distinct peaks corresponding to the two shear layers between the bluff-body recirculation region and the fuel jet and the air co-flow, respectively. The numerical predictions [Fig. 6] successfully capture first peak but second peak is somewhat underpredicted. Radial velocity fluctuations have been accurately predicted at all axial locations [Fig. 7].

The mixing field and combustion statistics are compared for the HM1 case. Three different grids coarse (85×191), medium (170×260) and fine (340×520) have been used to simulate HM1 case. Here only mixture fraction predictions using different grids are presented in Fig. 8 for comparison purposes. It can be seen that results from all three grids are identical and in good agreement with experiments. This suggests that the solution is grid independent and selection of the medium grid

(170×260) for further analysis is acceptable. Also Fig. 8 shows the effects of a constant ($C_{\varepsilon 1}$) modification in dissipation equation. The standard RSM ($C_{\varepsilon 1}=1.44$) predicts mixture fraction reasonably well up to x/D = 0.9 but then onwards severe over-prediction of spreading rate has resulted into significant underprediction of mixture fraction. While the modified RSM ($C_{\varepsilon 1}=1.6$) has shown slight underprediction of spreading rate up to x/D = 1.3 but much improved predictions can be seen at downstream positions. In Fig. 9 the rms fluctuations of mixture fraction values are compared. At the first three positions x/D = 0.26, 0.6 and 0.9 the peak values are slightly over-predicted but the positions of the peaks are captured very well by the calculations. Downstream predictions at x/D = 1.8, 2.4 show remarkably good agreement. It could be said that the overall mixing field results of Fig. 8 and 9 taken together are very good. This is mainly because we have considered detailed chemistry and used bulk velocity values at extended inlets instead of specifying speculative velocity profiles at the burner exit.

Using the mixing field predictions a conditional scalar dissipation rate $\widetilde{\chi}_{st}$ is calculated for each cell. Fig. 10 shows the profiles of $\widetilde{\chi}_{st}$ at different axial locations. Two peaks can be seen, one close to fuel inlet and other at the edge of the bluff-body and co-flow inlet. These peaks correspond to the shear layers and they diminish with increasing axial distance. Initially only one particle was considered and therefore a single passive scalar transport equation (Eq. 1) was solved. Later in the study the effects of multiple particles were investigated. Evolution of $\widetilde{I}_n$ within the domain was stored at each time step and used in conjunction with the conditional scalar dissipation field to compute a surface averaged conditional scalar dissipation rate $\hat{\chi}_{st,n}$, where *n* represent the particle number. The transient evolution of $\hat{\chi}_{st,1}$ is shown in Fig. 11. It can be seen that approximately after 40 ms the $\hat{\chi}_{st,1}$ reaches a steady state (≈ 2.34s^{-1}) and thereafter does not change with time. A single steady flamelet generated using the steady state value scalar dissipation rate of 2.34s^{-1} in conjunction with the GRI Mech 2.11, 3.0 and San Diego mechanisms and results were compared with conditional experimental measurements. The comparisons are shown in Fig. 12 and 13. All three mechanisms considered have produced similar results. It can be seen that overall the flamelet profiles accurately follow the experimental data for temperature and species in both fuel rich and lean zones. However the OH peak mass fraction has been

overpredicted and CO_2 profile shows some differences in the fuel rich region. These disagreements may have been resulted from uncertainties involved in the reaction mechanisms and other factors like the use of unity Lewis number assumption for all species. In this case conditional experimental data at different axial locations show very similar profiles hence the flame is not subjected to large changes of scalar dissipation rate. Therefore steady flamelet results of all the mechanisms have been calculated in the post-processing stage using a single flamelet (scalar dissipation rate equal to $2.34s^{-1}$).

The transient history of $\hat{\chi}_{st,1}$ is employed to obtain unsteady flamelet solution using the FlameMaster code. Here again three mechanisms GRI Mech 2.11, 3.0 and San Diego are used to study the influence of mechanisms. The initial condition was taken from a steady state solution (scalar dissipation rate equal to $1.85s^{-1}$) and initial nitrogen species concentrations (except N_2) were set to zero. Unsteady evolution of NO by all three mechanisms is shown in Fig. 14. The highest level of NO is generated by GRI Mech 3.0 almost double the amount of GRI Mech 2.11 and slightly higher than San Diego mechanism. Other species and temperature shown in Fig. 15 do not show a notable evolution with time as they have been initialised from a steady solution and show less sensitivity to the scalar dissipation rate changes. The radiation heat loss is accounted for in the unsteady calculations but has negligible effects on scalars. Results in Fig. 15 have been generated using GRI Mech 2.11 but very similar results (not shown here) have been obtained for the other two mechanisms.

Favre averaged temperature and species predicted by all three mechanisms are presented in Fig. 16-26. Results also compare performance of steady (SLFM) vs. unsteady (EPFM) flamelet model. Fig. 16 shows the temperature predictions. Temperature is slightly underpredicted at the centreline partly due to the discrepancies of mixture fraction predictions but generally the agreement is very good. Similar underprediction of temperature has been reported by Raman and Pitsch [29], who were successful in predicting the mixture fraction and concluded that this may be due to deviation from flamelet regime. Radiative heat transfer is not significant for the selected flame as the unsteady results with radiation and steady results without radiation are undistinguishable. All three mechanisms with both flamelet models provided almost identical results. Similar behaviour is seen in the case of temperature rms and other major species including OH, shown later. Comparison of calculated

temperature rms results are shown in Fig. 17. The downstream positions show some differences but overall agreement is very good. Successful modelling of temperature rms establishes that turbulence and chemistry interactions have been captured well.

Figure 18 shows present NO prediction which is the most challenging task in combustion simulations. It can be seen that the results of NO predictions by all three mechanisms are very different and noticeably affected by the choice of the flamelet model. Unsteady GRI Mech 2.11 shows the closest agreement with measurements. Although NO is slightly overpredicted at downstream locations by unsteady GRI 2.11 calculation, the results are very good. The steady flamelet model with GRI Mech 2.11 still predicts high NO levels and show overpredictions at all locations. The unsteady model incorporating the San Diego and GRI Mech 3.0 consistently overpredict NO levels at all the positions and steady flamelet results show even severe overpredictions. The GRI Mech 3.0 predicts roughly twice the amount of NO compared to GRI Mech 2.11. This finding supports the previous studies [23, 24]. The crucial prompt NO formation rate for CH + N2 = HCN + N was found by Berg *et al*. [42] to result in under-predictions of NO by 30 to 60%. Similarly, Juchmann *et al*. [43] found that the rate was significantly (~ 250%) too low when applied in the context of diffusion flames. Gibaud *et al.* [44] comment further on the differences between the two versions of the GRI mechanisms. They note that the rate constant used for the reaction CH_2+H = CH + H_2 which is the dominant CH formation channel is 2.06×10^{11} m^3/kmol/s in GRI Mech 2.11 and 1.71×10^{11} in GRI Mech 3.0 and note that the GRI Mech 2.11 rate is based on low-temperature data extrapolated to combustion conditions. Gibaud *et al.* [44] quoting references therein note that the reaction rate value for the temperature range 2200-2600 K varies from 3.2×10^{10} to 2.3×10^{11} m^3/kmol/s and the value used in GRI Mech 2.11 appears to be on the higher side. Juchmann *et al.* [43] and Gibaud *et al.* [44] have used a value of 1.1×10^{11} which is close to the value used in the GRI Mech 3.0. Considering these uncertainties the success of the GRI Mech 2.11 should be treated cautiously. However, our study clearly demonstrate the capability of the EPFM approach as the other two mechanisms, GRI 3.0 and San Diego, give better NO predictions compared to the SLFM approach.

Figure 19 shows the OH predictions by steady and unsteady methods incorporating all three mechanisms. At first position, x/D = 0.26 the OH mass fraction is severely overpredicted but further downstream results closely follow the

experimental data. Unsteady effects or different mechanisms do not show any significant difference. Figure 20 shows the carbon monoxide predictions which are in good agreement close to the burner but slightly overpredicted at downstream positions. Similar behaviour is seen in the case of carbon dioxide predictions shown in Fig. 21. The H_2O mass fraction predictions depicted in Fig. 22 shows excellent agreement at all the axial positions. Mass fraction of methane shown in Fig. 23 is also predicted well. Figure 24 show the comparison of predicted hydrogen mass fractions with data. Slight overprediction at the centre line is apparent which may be due to overprediction of mixture fraction at the centreline. Very good agreement can also be seen in Fig 25 for oxygen mass fraction predictions.

It can be seen that agreement with experimental results is very good for all species including temperature and not sensitive to unsteady effects except in the case of NO. All three mechanisms also produce remarkably similar results for major and minor species (except NO as mentioned above).

The unsteady results discussed so far have been obtained using a single particle. To study the impact of multiple particles on scalar predictions, another simulation was performed using five particles. In this case the actual computational time for the second stage calculations significantly increased from 3-4 hrs to 15-16 hrs. The NO predictions by a single particle and five particles employing unsteady GRI Mech 2.11 are shown in Fig. 26. The results are almost identical. Basically multiple particles help to account for the inhomogeneous distribution of scalar dissipation field. But the current flame has shown weak dependence on scalar dissipation rate in conditional data comparison discussed earlier and therefore results of five particles and a single particle are almost the same. Here only NO results are presented but similar trend has been seen in the case of temperature and other species (not shown here).

6. Conclusions

A methane/hydrogen bluff-body flame has been successfully simulated using steady and unsteady flamelet models. In this study Eulerian particles are traced using a post-processing style EPFM to consider the unsteady effects. Very good agreement of velocity statistics confirms the ability of the RSM based axisymmetric RANS approach to model such a strongly recirculating flame. The upstream domain

extension has allowed the use of bulk velocity values at extended inlet instead of prescribing velocity profiles at the burner exit. This has eliminated uncertainties arising from the velocity boundary condition. The mean and variance of mixture fraction were predicted correctly, which show the validity of the laminar flamelet model for this study. The predicted temperature profiles using the steady and unsteady laminar flamelet approaches agreed well with experiments even at far downstream positions. It was found that the radiative heat loss is not significant for the current flame as temperature predictions by steady calculations without radiation and unsteady calculations with radiation were almost the same. The good agreement shown by temperature rms reveals that chemistry (using laminar flamelet model) and turbulence-chemistry interactions (using presumed β-PDF) were modelled well. The major species and OH predictions by all three mechanisms (GRI Mech 2.11, 3.0 and San Diego) using steady and unsteady flamelets were very similar and agreed well with experimental data. However, the results of this study show that nitrogen oxide predictions are highly sensitive to the unsteady effects and the mechanism considered. Only unsteady calculations employing GRI Mech 2.11 showed reasonable agreement for NO predictions. Results showed overpredictions even with the GRI Mech 2.11 when transient effects were neglected. The other two mechanisms namely San Diego and GRI Mech 3.0 using unsteady flamelets predicted higher level of NO compared to unsteady GRI Mech 2.11 and showed severe over-predictions when steady flamelet approach was used. The GRI Mech 3.0 consistently predicted double the amount of NO compared to GRI Mech 2.11. The NO predictions by San Diego mechanism resulted values between two GRI Mech predictions. The conditional experimental data has shown that the current flame does not strongly depend on scalar dissipation rate and therefore a single flamelet in the case of steady flamelet model and a single particle calculation in the case of unsteady flamelet model were sufficient to simulate the flame accurately.

Acknowledgements

Authors are very grateful to Prof. H. Pitsch and his research group for providing FlameMaster code and assistance to use it. Authors would also like to thank Prof. P. J. Coelho for valuable discussions of the Eulerian Particle Flamelet Model.

References

[1] N. Peters, Progress Energy Combust. Sci. 10 (1984) 319-339.

[2] N. Peters, Proc. Combust. Inst. 21 (1986) 1231-1250.

[3] N. Peters, Turbulent Combustion, Cambridge Univ. Press, London/New-York, 2000, p. 212.

[4] S.B. Pope, Prog. Energy Combust. Sci. 11 (1985) 119-192.

[5] A.Y. Klimenko, Fluid Dynamics 25 (1990) 327-334.

[6] R.W. Bilger, Phys. Fluids A 5 (1993) 436-444.

[7] D.C. Haworth, M.C. Drake, S.B. Pope, and R.J. Blint, Proc. Combust. Inst. 22 (1988) 589-597.

[8] F. Mauss, D. Keller, and N. Peters, Proc. Combust. Inst. 23 (1990) 693-698.

[9] H. Pitsch, Y.P. Wan, N. Peters, SAE Paper 952357 (1995).

[10] H. Pitsch, H. Barths, N. Peters, SAE Paper 962057 (1996).

[11] H. Barths, C. Antoni, N. Peters, SAE Paper 982459 (1998).

[12] H. Pitsch, M. Chen, and N. Peters, Proc. Combust. Inst. 27 (1998) 1057-1064.

[13] Y.P. Wan, H. Pitsch, N. Peters, SAE Paper 971590 (1997).

[14] H. Barths, N. Peters, N. Brehm, A. Mack, M. Pfitzner, and V. Smiljanovski, Proc. Combust. Inst. 27 (1998) 1841-1847.

[15] P.J. Coelho, and N. Peters, Combust. Flame 124 (2001) 444-465.

[16] P.J. Coelho, and N. Peters, Combust. Flame 124 (2001) 503-518.

[17] B.B. Dally, A.R. Masri, R.S. Barlow, G.J. Fietchner, Combust. Flame 114 (1998) 119-148.

[18] B.B. Dally, D.F. Fletcher, and A.R. Masri, Combust. Theory Modelling 2 (1998) 193-219.

[19] G. Li, B. Naud, and D. Roekaerts, Flow, Turbulence and Combustion 70 (2003) 211-240.

[20] J. Yan, F. Thiele, and M. Buffat, Flow, Turbulence and Combustion 73 (2004) 1-24.

[21] M. Hossain and W. Malalasekera, Proc. Inst. Mech. Engrs. Vol. 217, Part A: J Power and Energy (2003) 201-210.

[22] M. Hossain, J.C. Jones and W. Malalasekera, Flow Turbulence and Combustion 67 (2001) 217-234.

[23] S.H. Kim, K.Y. Huh, Combust. Flame 130 (2002) 94-111.

[24] S. Sreedhara, K. Y. Huh, Combust. Flame 143 (2005) 119-134.
[25] M. Muradoglu, K. Liu, S.B. Pope, Combust. Flame 132 (2003) 115-137.
[26] K. Liu, S.B. Pope, D.A. Caughey, Combust. Flame 141 (2005) 89-117.
[27] T.S. Kuan, R.P. Lindstedt, Proc. Combust. Inst. 30 (2005) 767-774.
[28] A. Kempf, R.P. Lindstedt, J. Janicka, Combust. Flame 144 (2006) 170-189.
[29] V. Raman, H. Pitsch, Combust. Flame 142 (2005) 329-347.
[30] B.E. Launder, Inter. J. Heat Fluid Flow 10 (1989) 282-300.
[31] B.E. Launder, Inter. J. Num. Methods in Fluids 9 (1989) 963-985.
[32] H. Pitsch, A C++ Computer Program for 0-D and 1-D Laminar Flame Calculations, RWTH Aachen (1998).
[33] H. Pitsch, N. Peters, Combust. Flame 114 (1998) 26-40.
[34] W.P. Jones, J.H. Whitelaw, Combust. Flame 48 (1982) 1-26.
[35] H. Barths, C. Hasse, G. Bikas and N. Peters, Proc. Combust. Inst. 28 (2000) 1161-1168.
[36] TNF6 Bluff-body flames, Experimental data can be downloaded at: http://www.mech.eng.usyd.edu
[37] C.T. Bowman, R.K. Hanson, D.F. Davidson, W.C. Gardiner, Jr., V. Lissianski, G.P. Smith, D.M. Golden, M. Frenklach and M. Goldenberg, http://www.me.berkeley.edu/gri_mech/
[38] Gregory P. Smith, David M. Golden, Michael Frenklach, Nigel W. Moriarty, Boris Eiteneer, Mikhail Goldenberg, C. Thomas Bowman, Ronald K. Hanson, Soonho Song, William C. Gardiner, Jr., Vitali V. Lissianski, and Zhiwei Qin http://www.me.berkeley.edu/gri_mech/
[39] San Diego Mechanism website, http://maeweb.ucsd.edu/combustion/cermech/
[40] TNF workshop website, http://www.ca.sandia.gov/TNF/radiation.html
[41] FLUENT Manual http://www.fluentusers.com
[42] P.A. Berg, G.P. Smith, J.B. Jeffries and D.R. Crosley, Proc. Comb. Inst., 27, (1998), 1377-1384.
[43] W. Juchmann, H. Latzel, D.I. Shin, G. Peiter, T. Dreiter, H.R. Volpp, J. Wolfrum, R.P. Lindstedt, and K.M. Leung., Proc. Combut. Inst, 27 (1998), 469-476.
[44] C. Gibuad, J.A. Snyder, V. Sick, and R.P. Lindstedt, Proc. Comb. Inst., 30 (2005), 455-463.

Figure Captions

Figure 1 Axisymmetric grid used in the simulations.

Figure 2 The EPFM algorithm.

Figure 3 The streamline contours: (a) HM1e case, (b) HM1 case.

Figure 4 Comparison of axial velocity with experimental data at different axial stations.

Figure 5 Comparison of radial velocity with experimental data at different axial stations.

Figure 6 Comparison of axial velocity rms with experimental data at different axial stations.

Figure 7 Comparison of radial velocity rms with experimental data at different axial stations.

Figure 8 Comparison of mean mixture fraction with experimental data at different axial stations.

Figure 9 Comparison of mean mixture fraction rms with experimental data at different axial stations.

Figure 10 Conditional scalar dissipation rate values at different axial positions.

Figure 11 Transient evolution of a surface averaged conditional scalar dissipation rate in case of a single particle.

Figure 12 Comparison of conditional experimental data with flamelet profiles.

Figure 13 Comparison of conditional experimental data with flamelet profiles.

Figure 14 Transient evolution of NO using different chemical mechanisms.

Figure 15 Transient evolution of temperature and other species using GRI Mech 2.11.

Figure 16 Comparison of temperature profiles with experimental data at different axial stations.

Figure 17 Comparison of temperature rms profiles with experimental measurements at different axial locations.

Figure 18 Comparison of NO mass fraction profiles with experimental data at different axial positions.

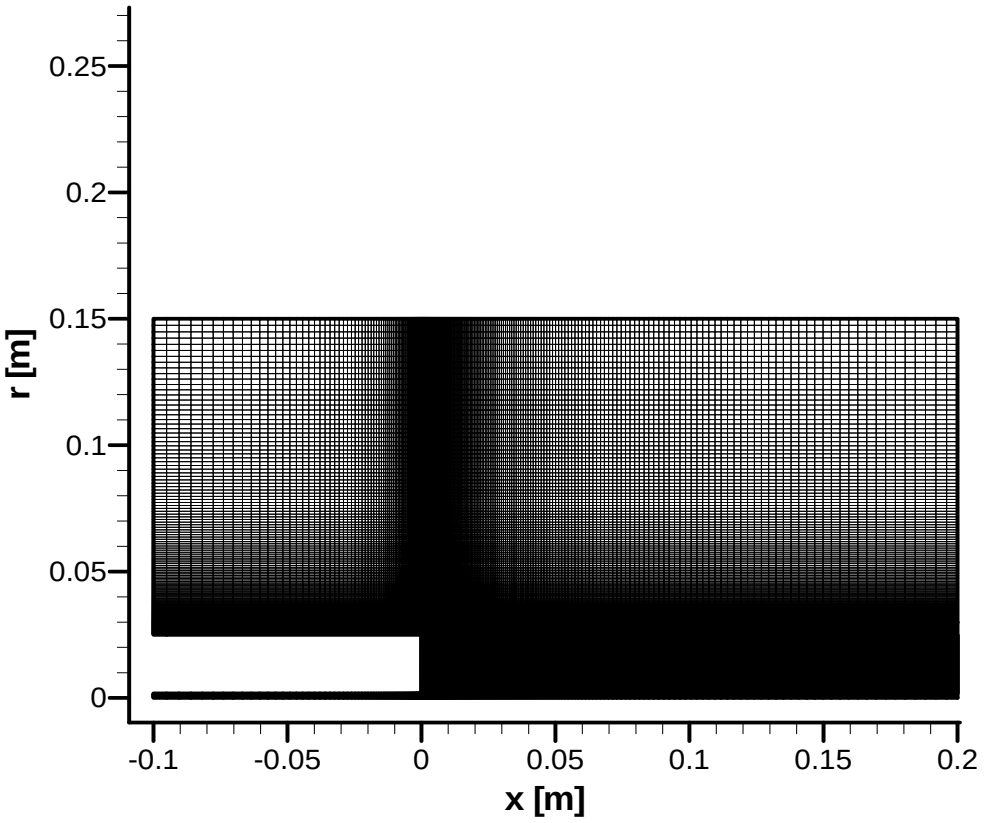

Figure 1

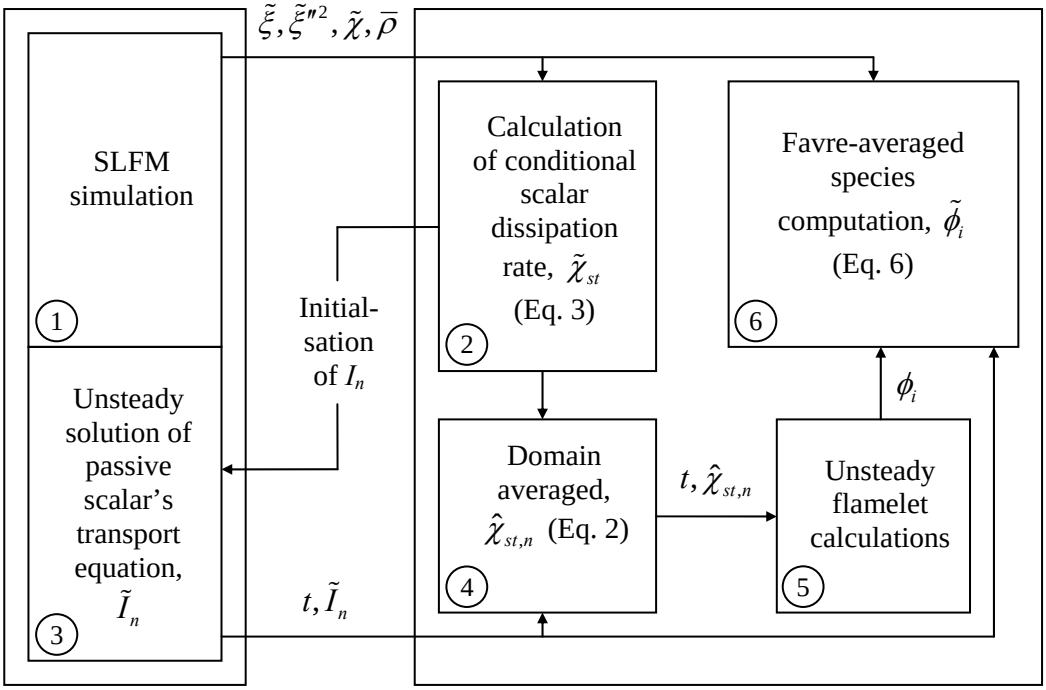
$\tilde{\xi}, \tilde{\xi}''^2, \tilde{\chi}, \bar{\rho}$
SLFM simulation
1
Unsteady solution of passive scalar's transport equation, $\tilde{I}_n$
3
Initial-sation of I_n
$t, \tilde{I}_n$
Calculation of conditional scalar dissipation rate, $\tilde{\chi}_{st}$ (Eq. 3)
2
Domain averaged, $\hat{\chi}_{st,n}$ (Eq. 2)
4
$t, \hat{\chi}_{st,n}$
Unsteady flamelet calculations
5
Favre-averaged species computation, $\tilde{\phi}_i$ (Eq. 6)
6
ϕ_i
CFD Calculations
Post-processing EPFM

Figure 2

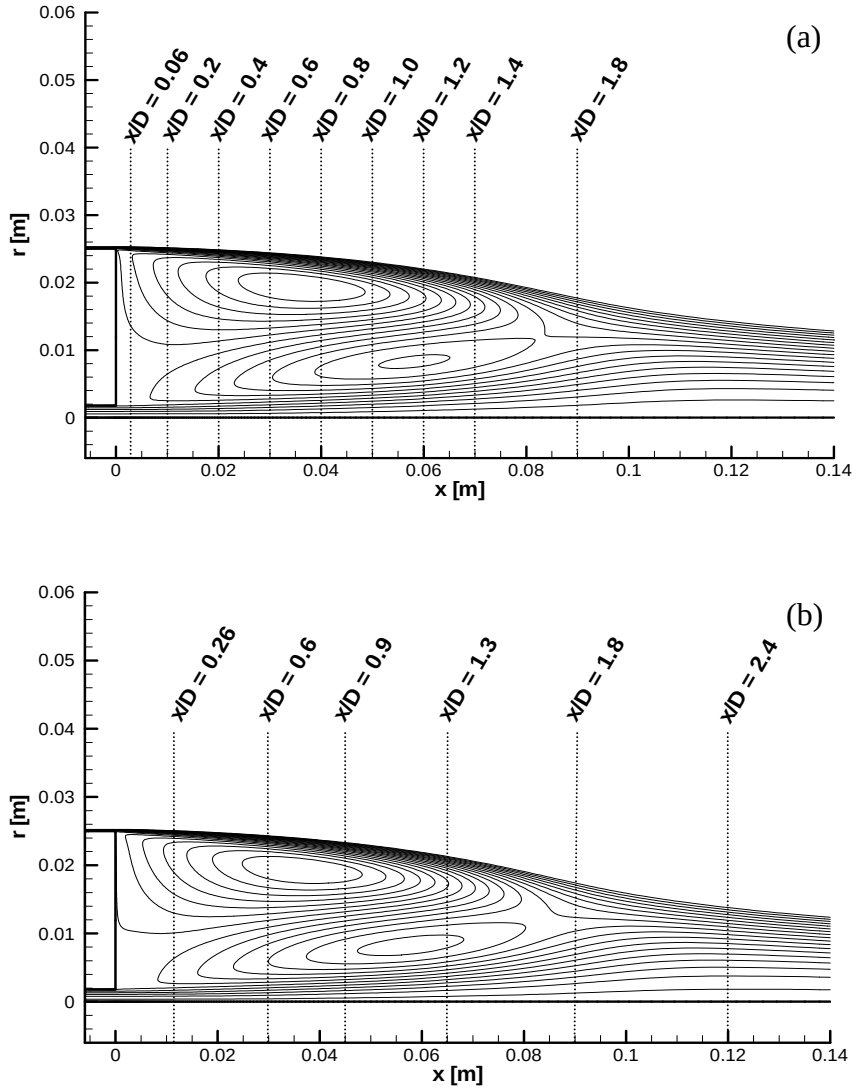
(a)
x/D = 0.06
x/D = 0.2
x/D = 0.4
x/D = 0.6
x/D = 0.8
x/D = 1.0
x/D = 1.2
x/D = 1.4
x/D = 1.8
r [m]
x [m]
0.06
0.05
0.04
0.03
0.02
0.01
0
0.02
0.04
0.06
0.08
0.1
0.12
0.14
(b)
x/D = 0.26
x/D = 0.6
x/D = 0.9
x/D = 1.3
x/D = 1.8
x/D = 2.4
r [m]
x [m]

Figure 3

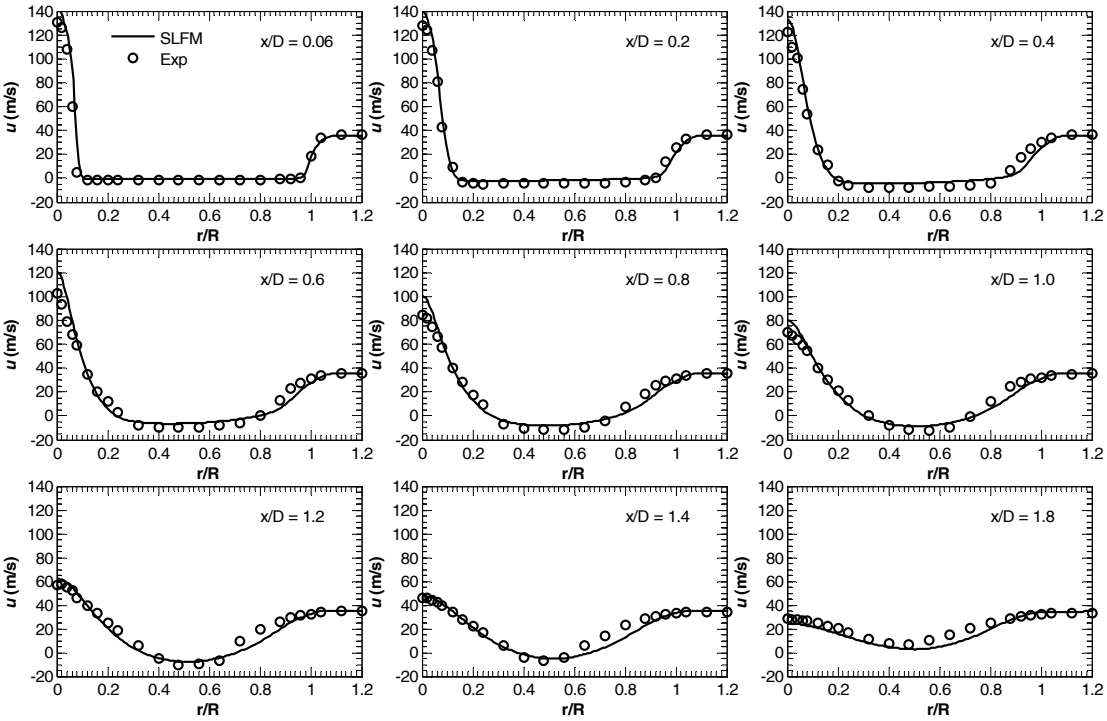

Figure 4

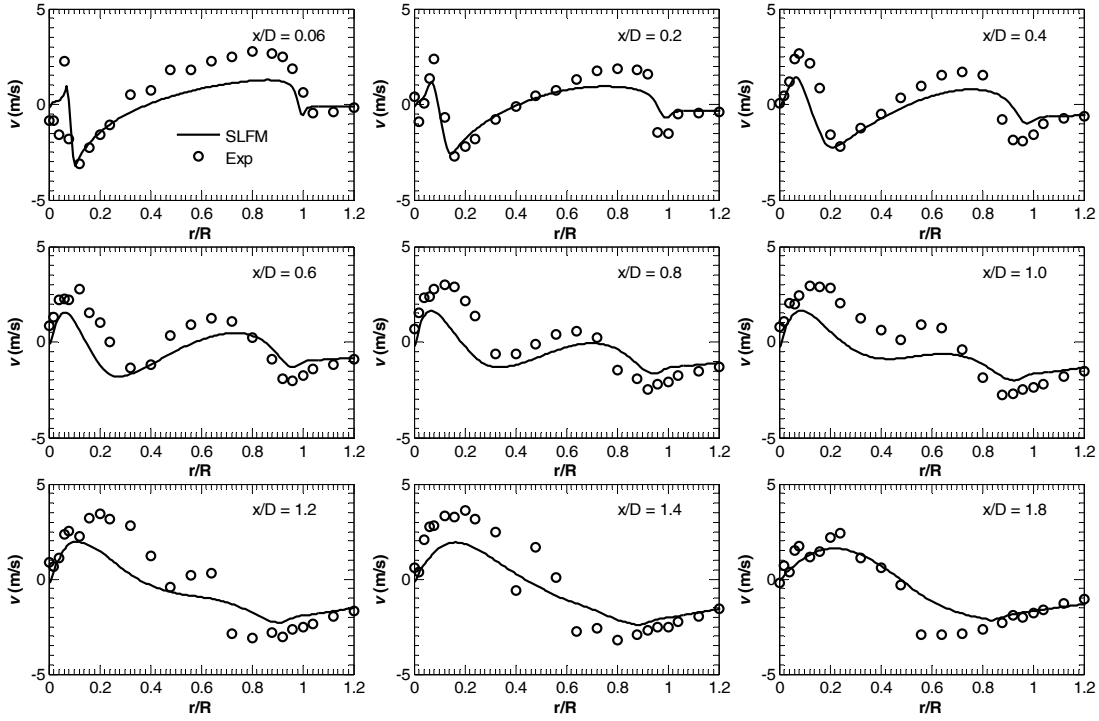

Figure 5

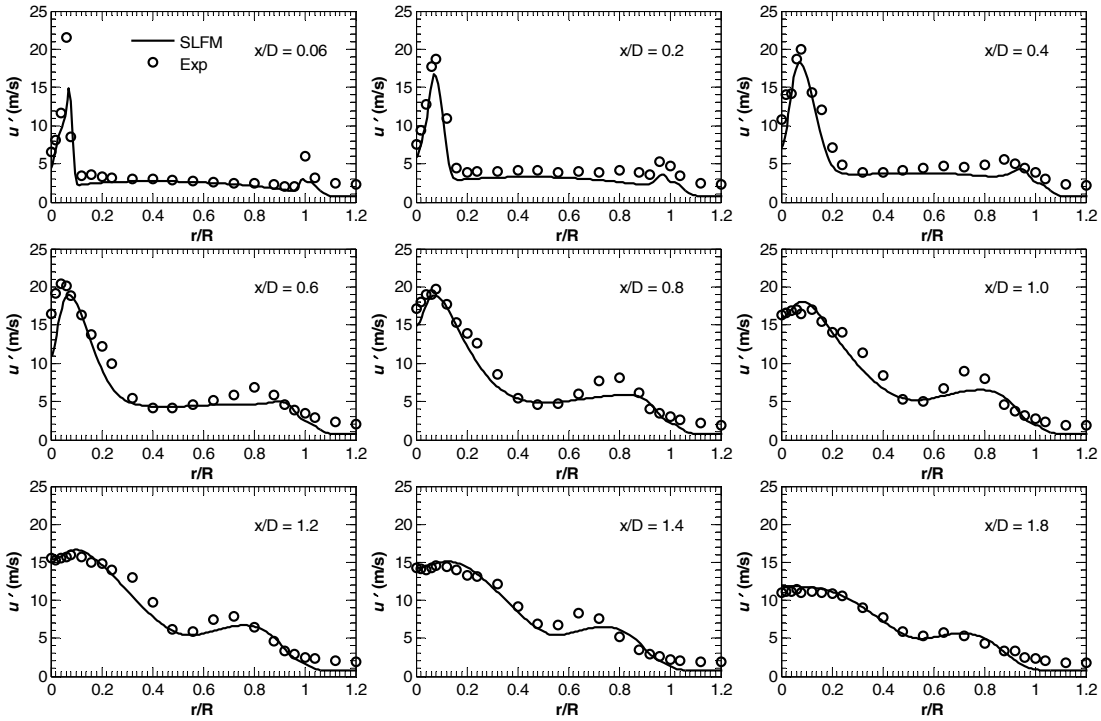

Figure 6

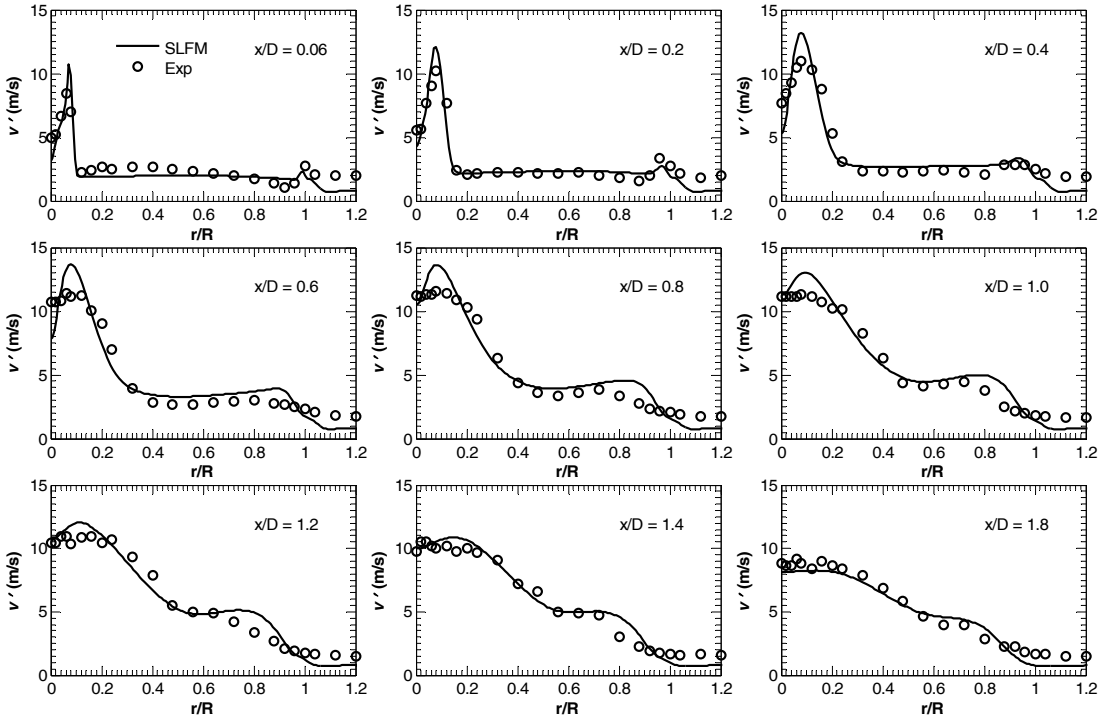

Figure 7

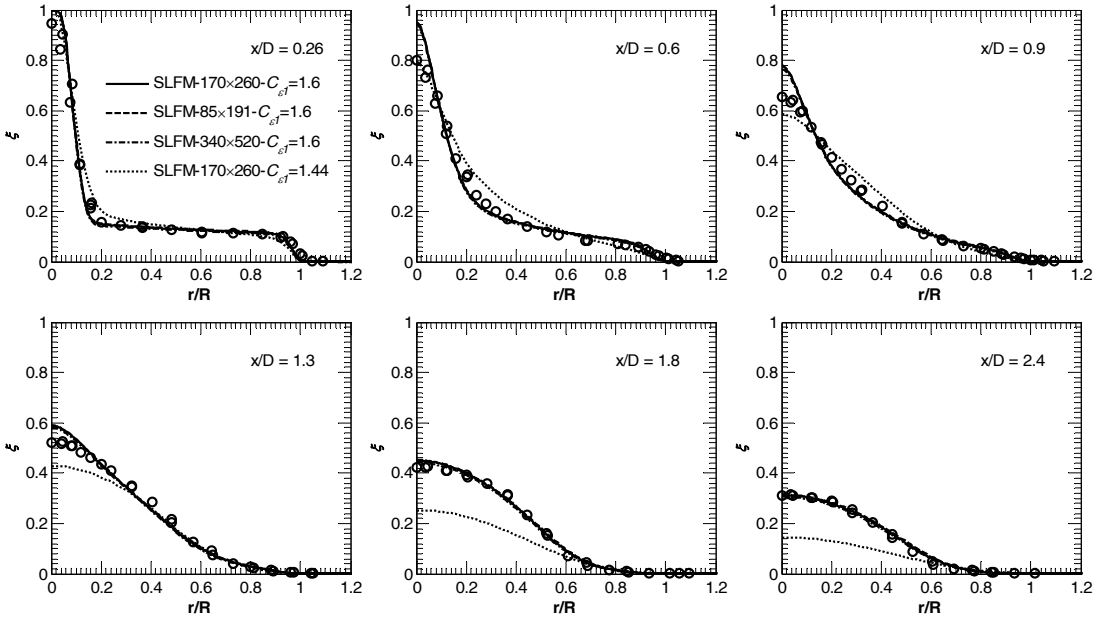

Figure 8

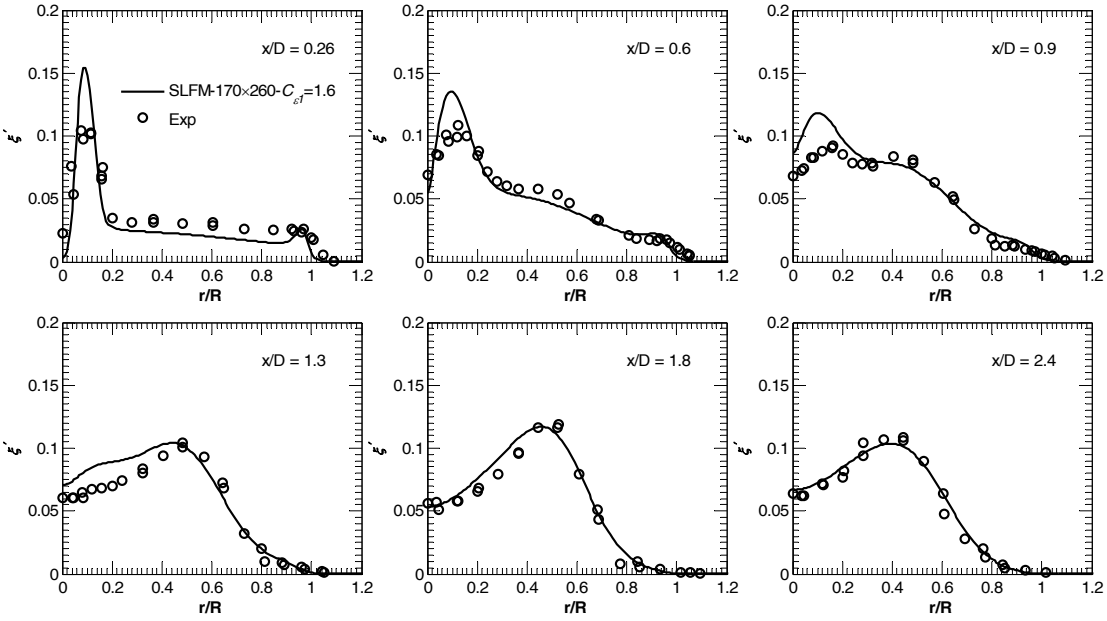

Figure 9

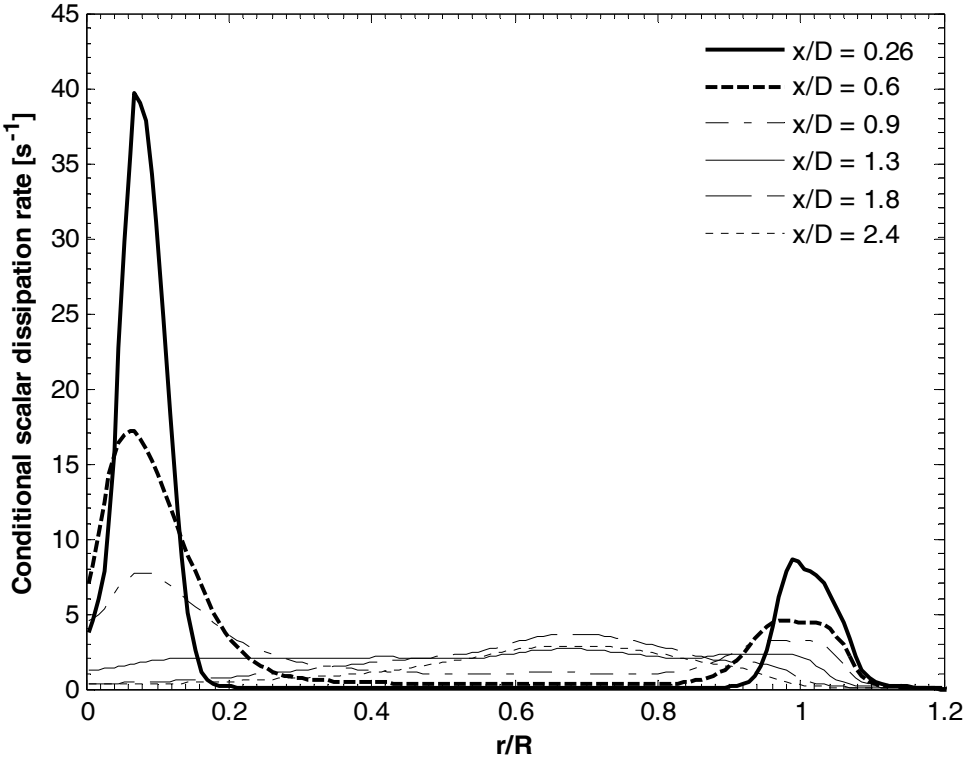

Figure 10

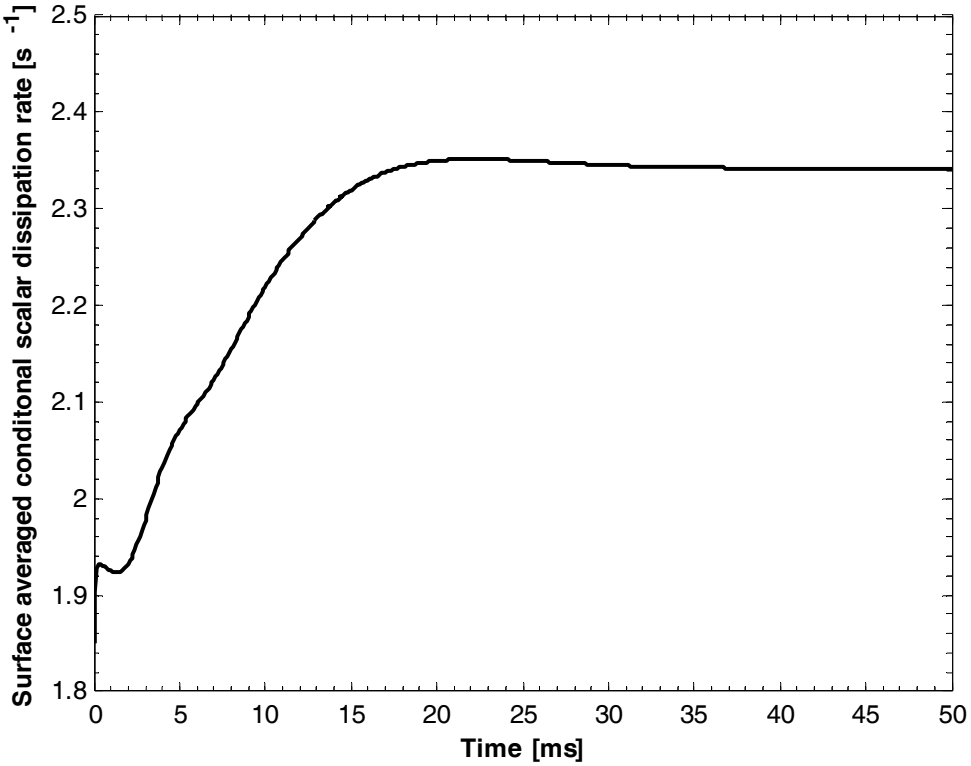

Figure 11

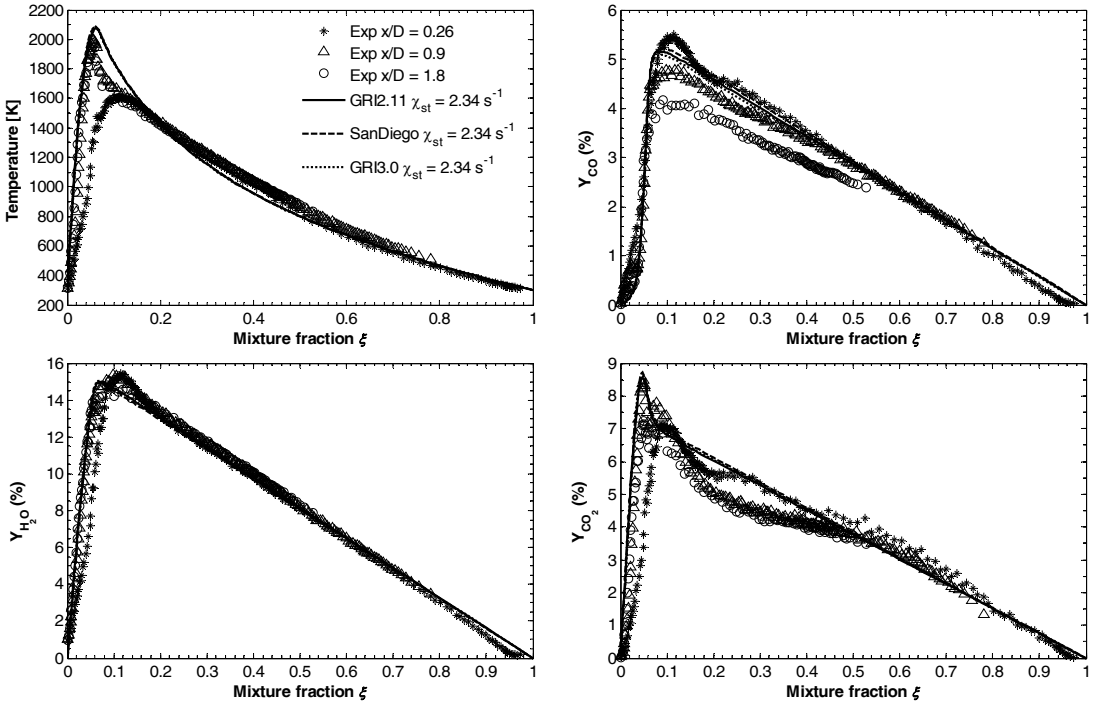

Figure 12

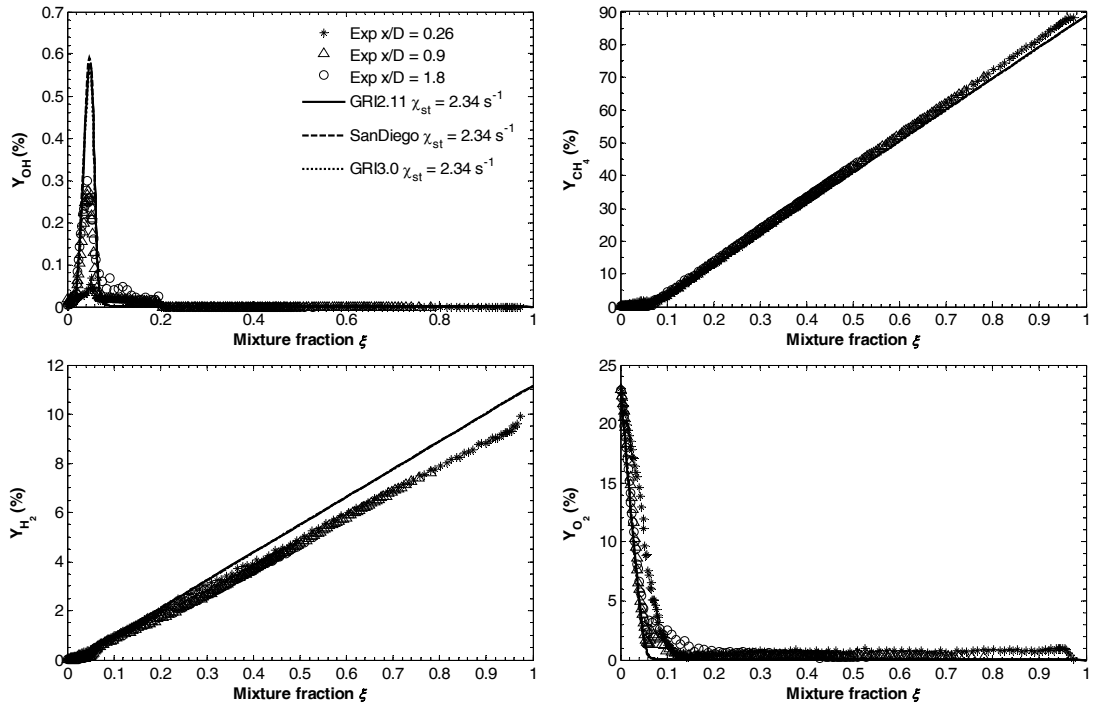

Figure 13

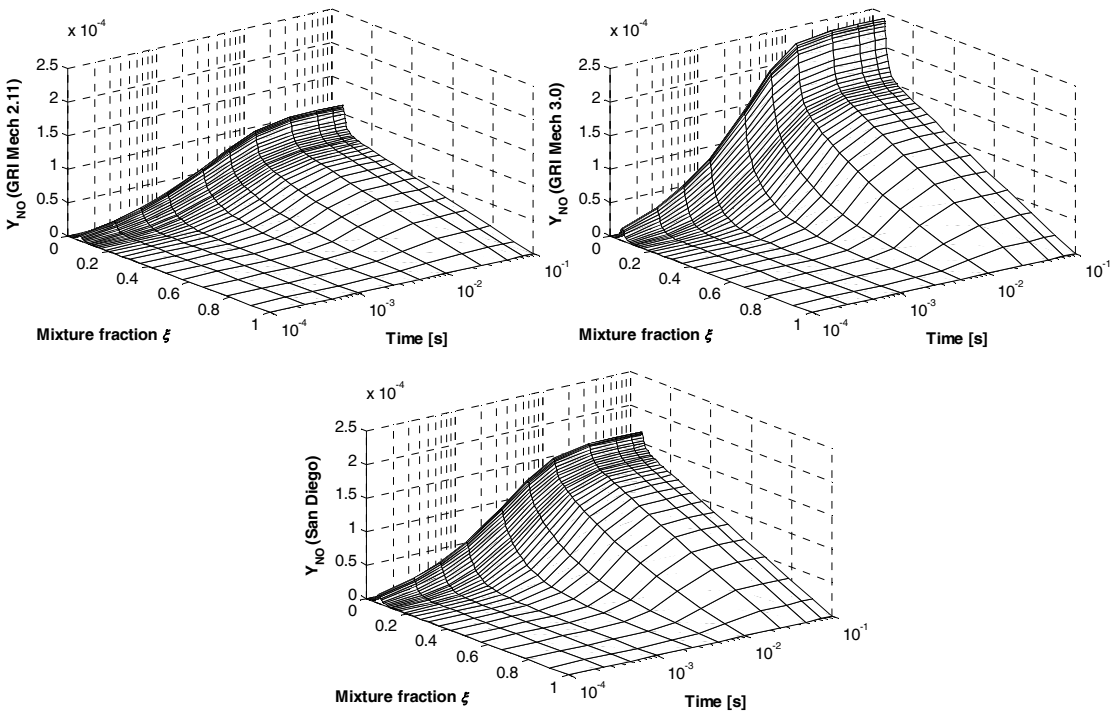

Figure 14

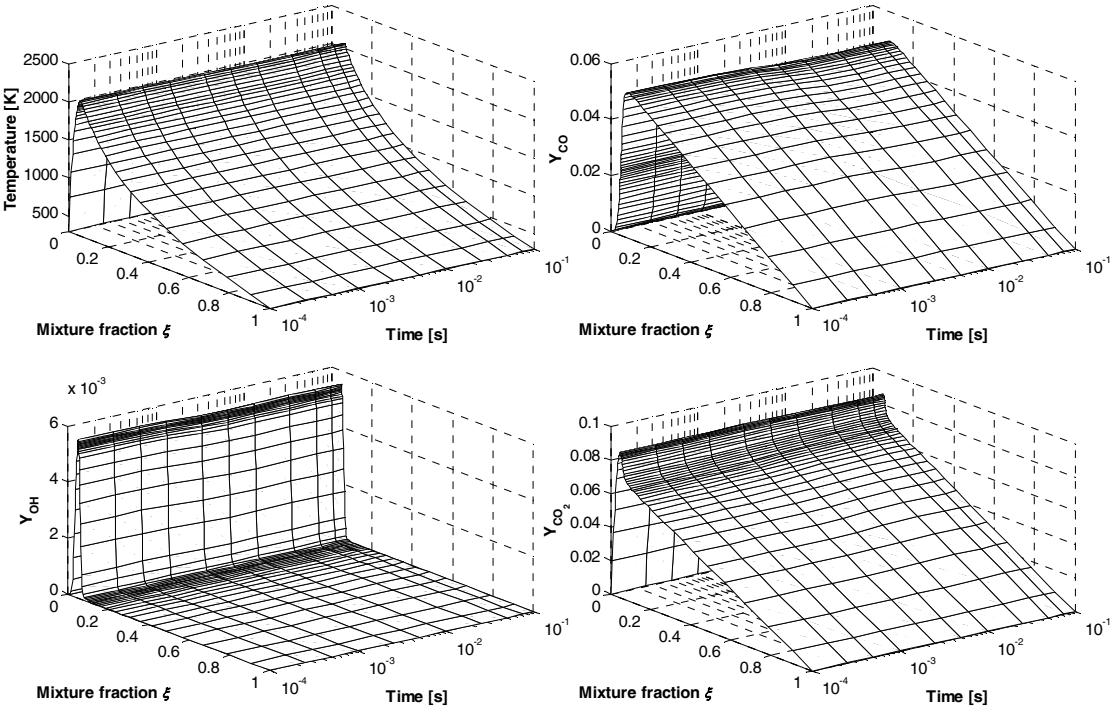

Figure 15

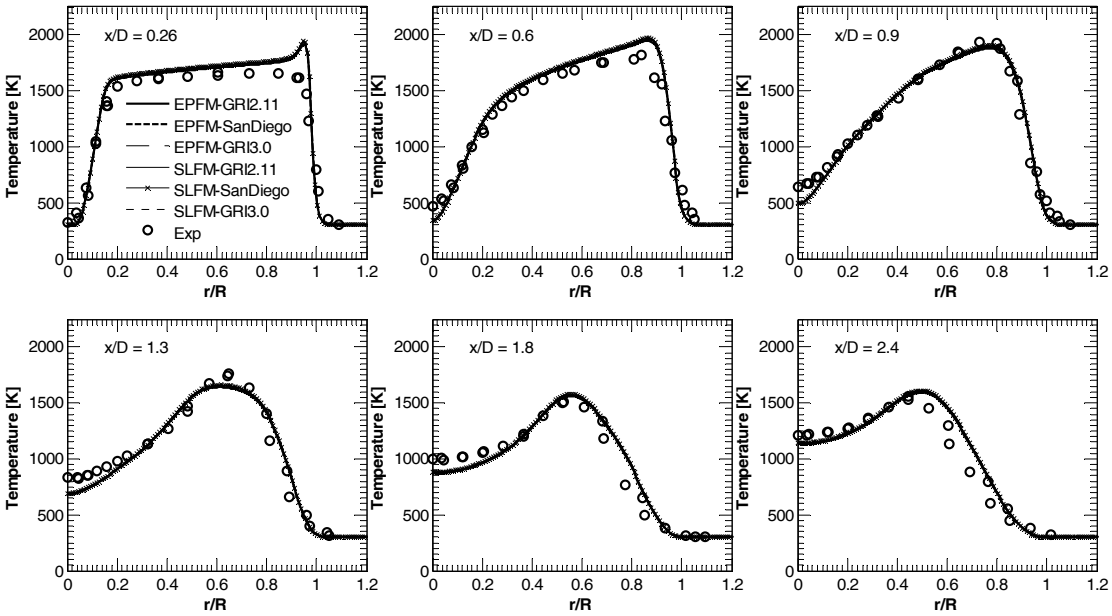

Figure 16

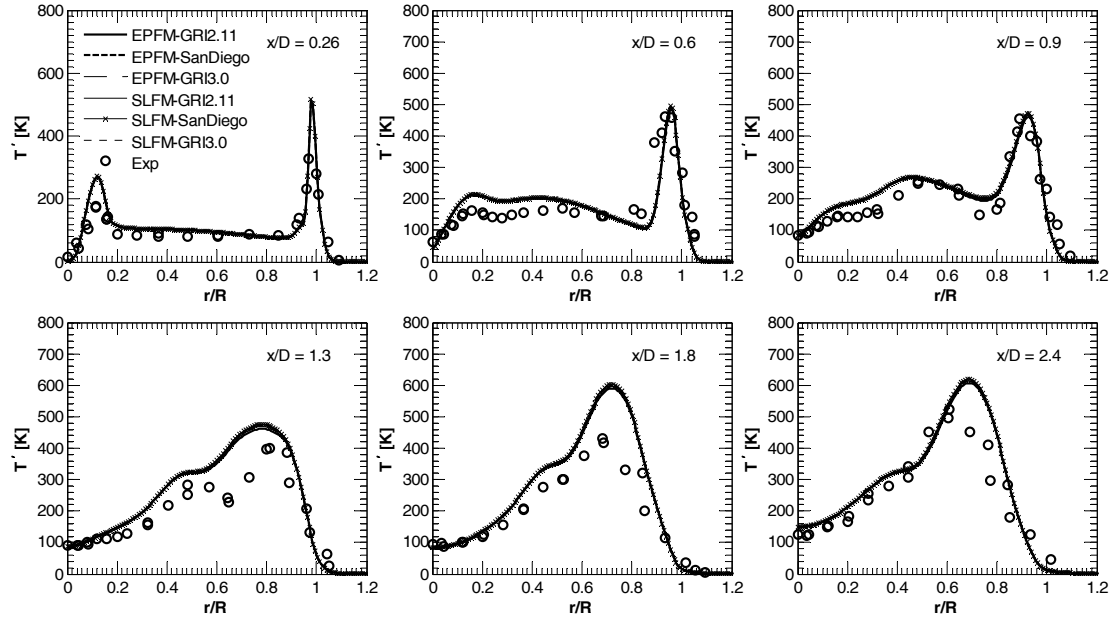

Figure 17

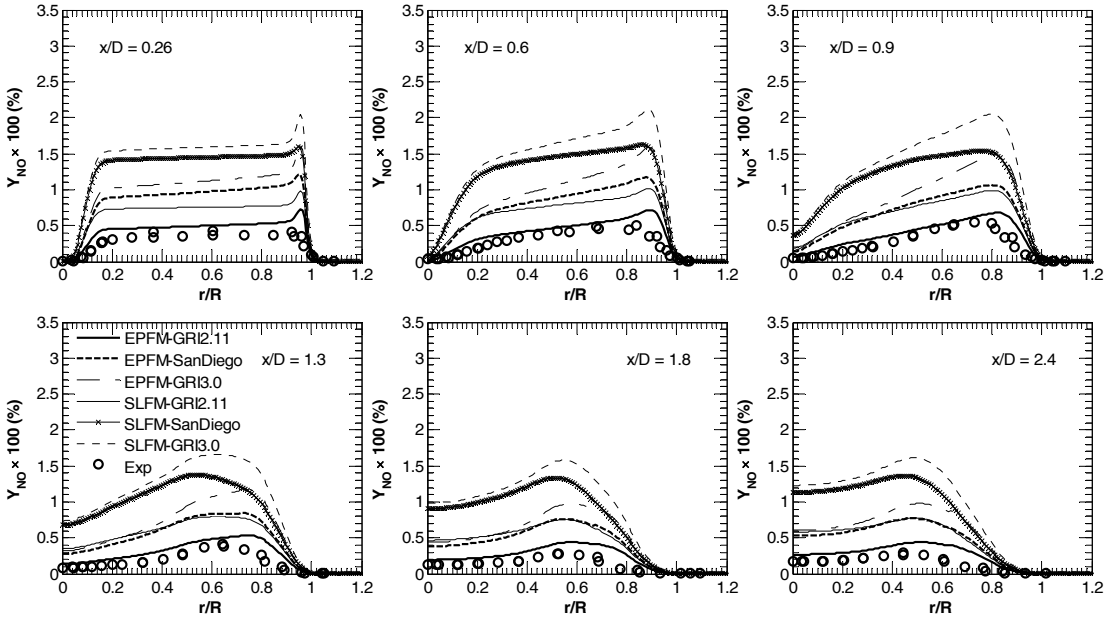

Figure 18

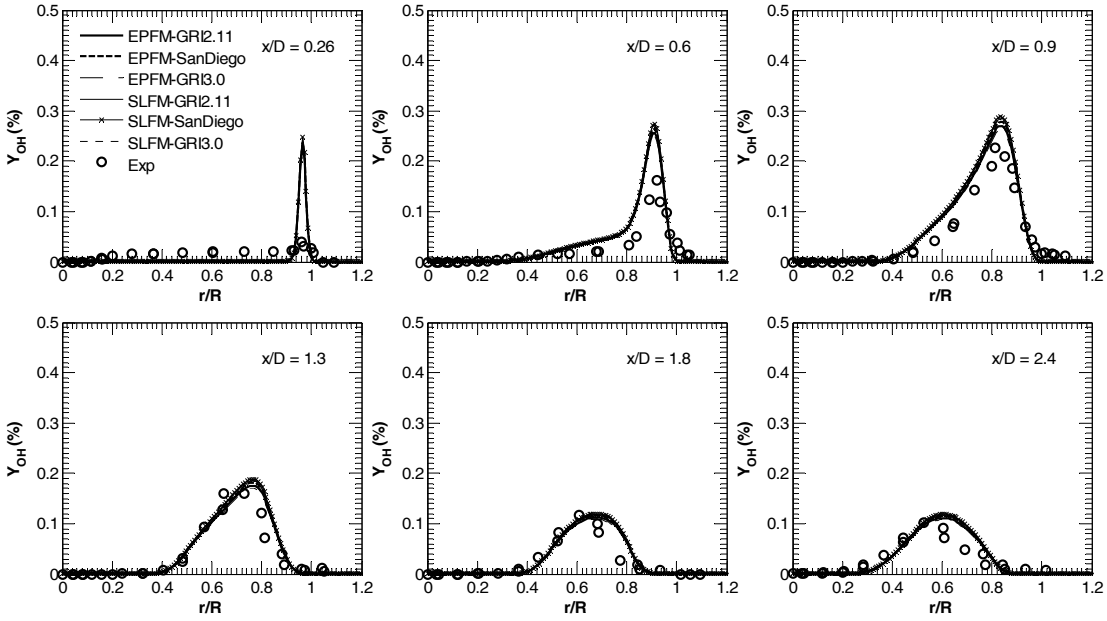

Figure 19

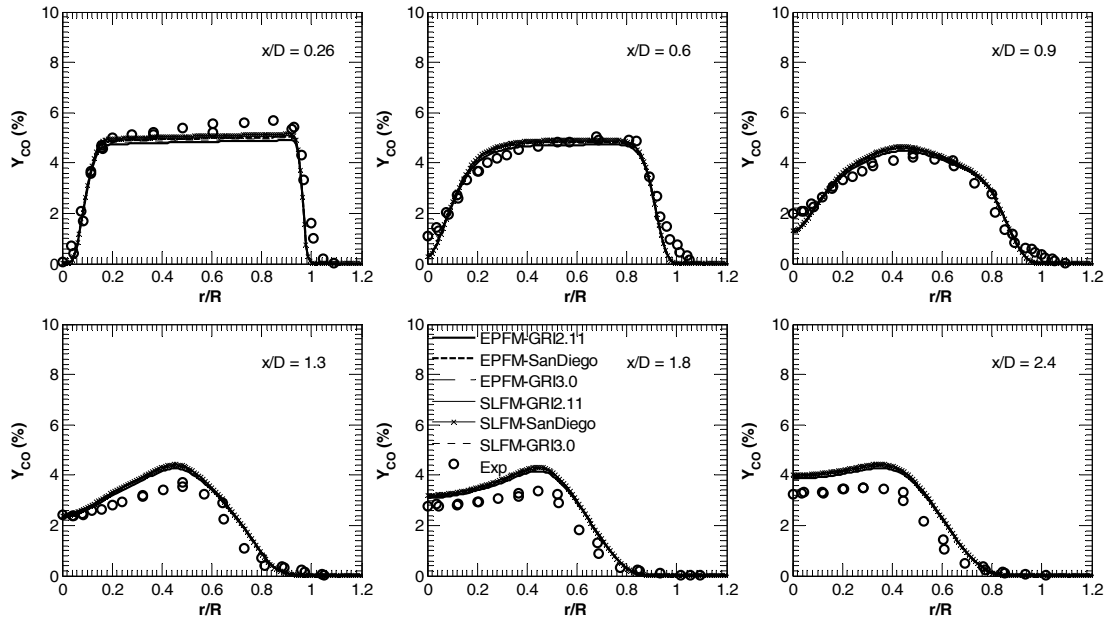

Figure 20

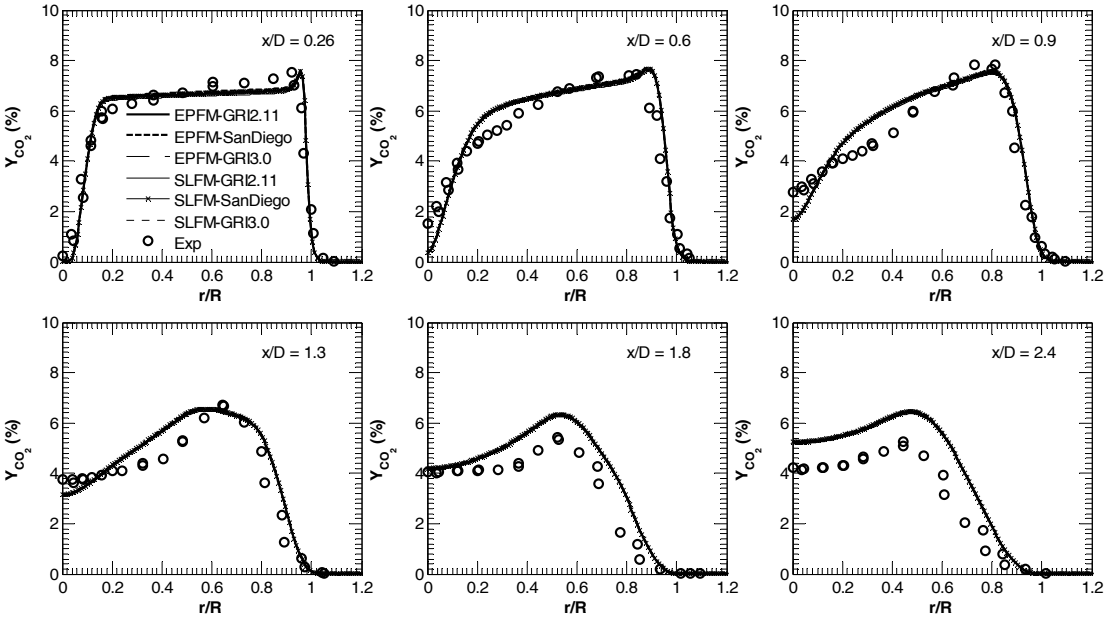

Figure 21

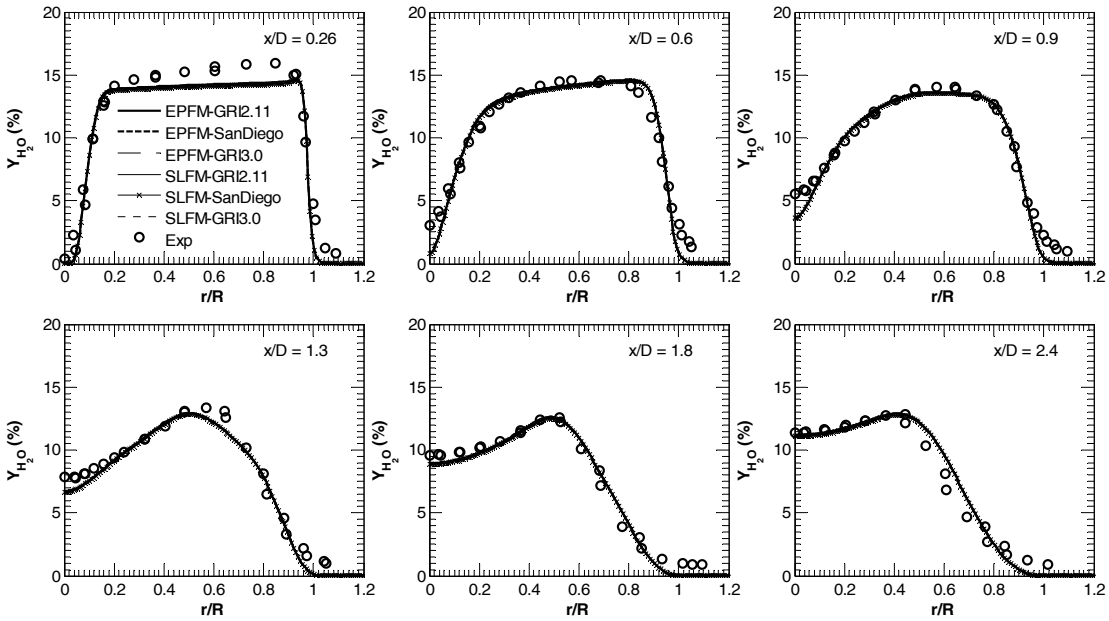

Figure 22

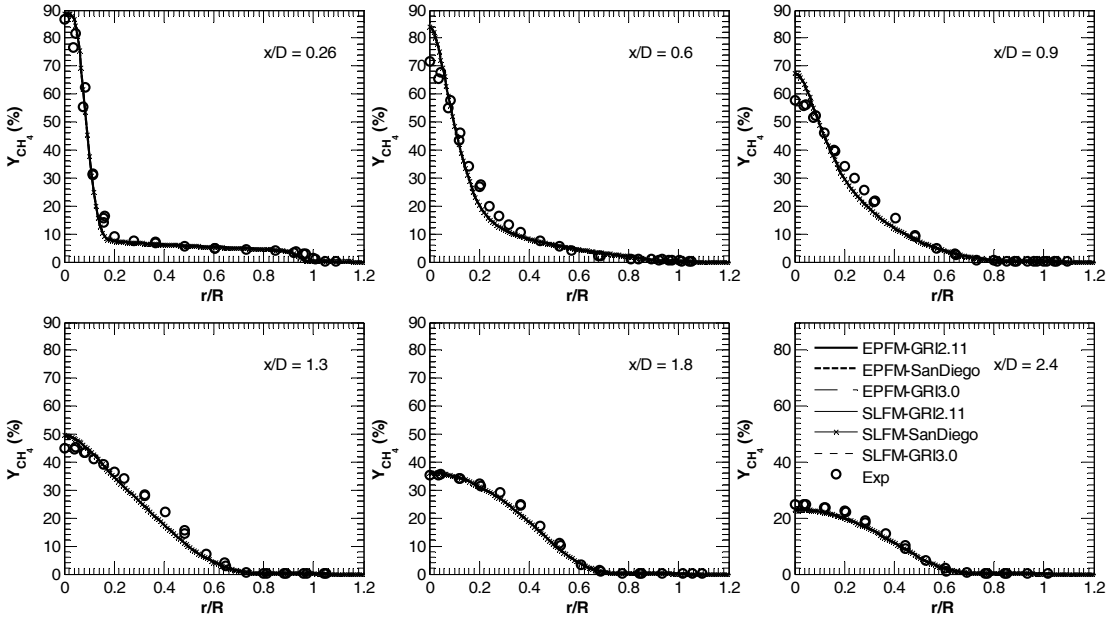

Figure 23

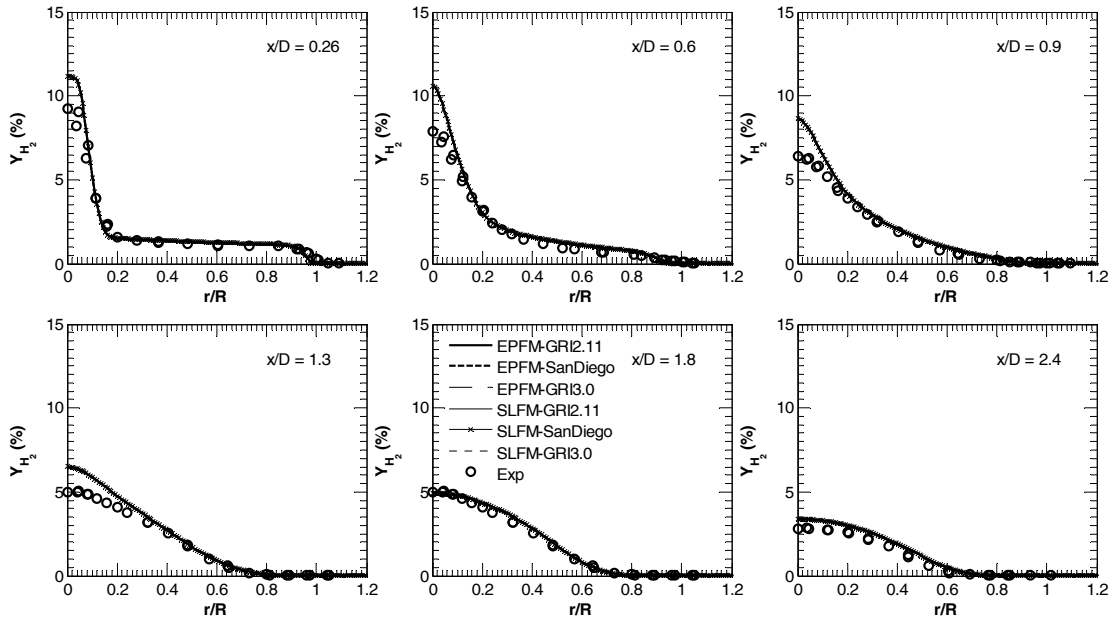

Figure 24

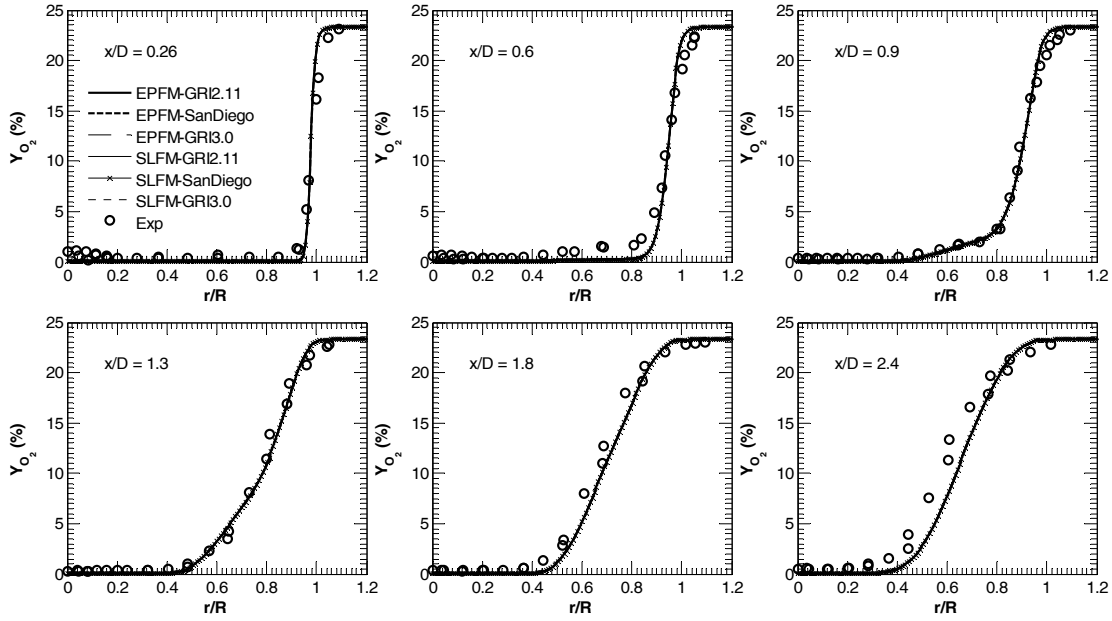

Figure 25

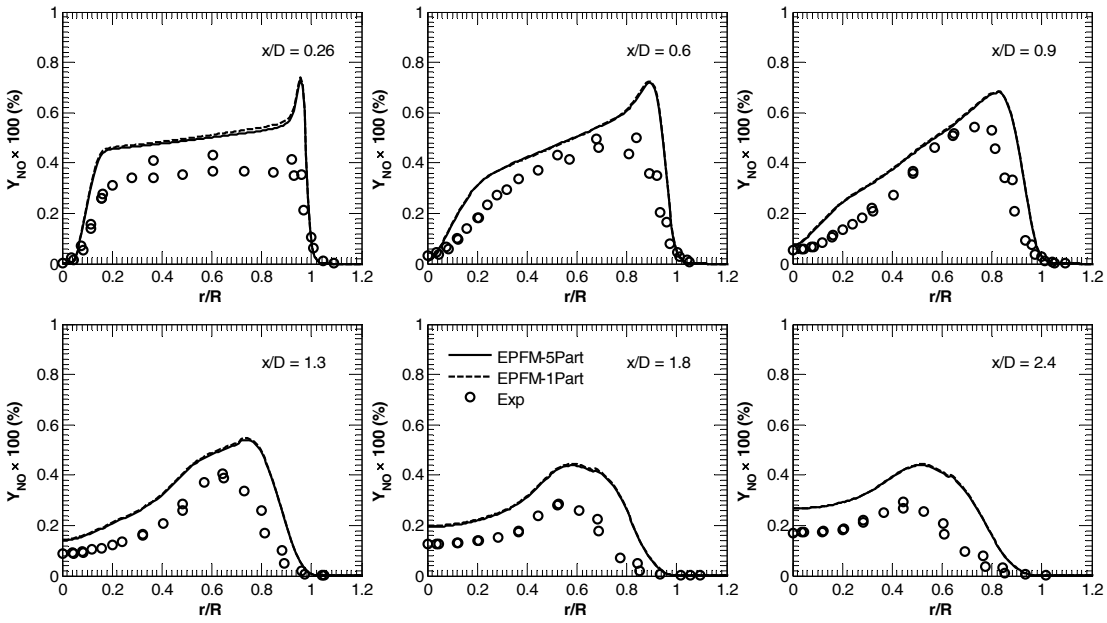
x/D = 0.26
x/D = 0.6
x/D = 0.9
x/D = 1.3
x/D = 1.8
x/D = 2.4
EPFM-5Part
EPFM-1Part
Exp
$Y_{NO} \times 100$ (%)
r/R

Figure 26